Northern high-latitude permafrost and terrestrial carbon response to solar geoengineering

Yangxin Chen[1], Duoying Ji[1], Qian Zhang[1], John C. Moore[1,2,3], Olivier Boucher[4], Andy Jones[5], Thibaut Lurton[4], Michael J. Mills[7], Ulrike Niemeier[8], Roland Séférian[6], and Simone Tilmes[7]

5 [1]College of Global Change and Earth System Science, Beijing Normal University, Beijing, China

[2]CAS Center for Excellence in Tibetan Plateau Earth Sciences, Beijing, China

[3]Arctic Centre, University of Lapland, Rovaniemi, Finland

[4]Institut Pierre-Simon Laplace, Sorbonne Université/CNRS, Paris, France

[5]Met Office Hadley Centre, Exeter, EX1 3PB, UK

10 [6]CNRM, Université de Toulouse, Météo-France, CNRS, Toulouse, France

[7]Atmospheric Chemistry, Observations, and Modeling Laboratory, National Center for Atmospheric Research, Boulder, CO, USA

[8]Max Planck Institute for Meteorology, Hamburg, Germany

Correspondence to: Duoying Ji (duoyingji@bnu.edu.cn)

15 **Abstract.**

The northern high-latitude permafrost contains almost twice the carbon content of the atmosphere, and it is widely considered as a non-linear and tipping element in the Earth's climate system under global warming. Solar geoengineering is a means of mitigating temperature rise and reduce some of the associated climate impacts by increasing the planetary albedo, including permafrost thaw. We analyze the permafrost response as simulated by five earth system models (ESMs) under four future

20 scenarios; two solar geoengineering scenarios (G6solar and G6sulfur) restore the global temperature from the high emission scenario (ssp585) levels to the moderate mitigation scenario (ssp245) levels via solar dimming and stratospheric aerosol injection. G6solar and G6sulfur nearly restore the northern high-latitude permafrost area from ssp585 levels to those under ssp245. But deeper active layer thickness and more exposed unfrozen soil organic carbon are produced due to robust residual high-latitude warming, especially over Eurasia. However, G6solar and G6sulfur accumulate more soil carbon over the northern

25 high-latitude permafrost region due to enhanced CO_2 fertilization effects relative to ssp245 and weakened heterotrophic respiration relative to ssp585. The asynchronous changes in soil carbon inputs and soil carbon decomposition directly result from decoupling of temperature and atmospheric CO_2 concentration under solar geoengineering. The permafrost ecosystem remains a carbon sink throughout this century under all four scenarios, and solar geoengineering can delay the transition of northern high-latitude permafrost ecosystem from carbon sink to carbon source.

30 **1 Introduction**

The extent of northern high-latitude permafrost is estimated to be 12.9-17.8 million km[2] and accounts for 9-14 percent of the exposed land surface area (Gruber, 2012). The carbon content of permafrost is nearly twice that of the atmosphere (Tarnocai

et al., 2009), with approximately 1035 Pg organic carbon stored in the upper 3 m of soil (Hugelius et al., 2014), accounting for roughly half of the global soil carbon (Strauss et al., 2017). In the past several decades, the northern high-latitude experienced

35 greater warming than the lower latitudes, and this rapid warming trend is expected to continue in the future, driven by Arctic amplification (Serreze et al., 2011; Biskaborn et al., 2019). Continued climate warming over the northern high latitudes, accelerated microbial decomposition and higher climatological temperature sensitivity of soil carbon in cold regions (Schuur et al., 2008; Koven et al., 2017) renders the permafrost soil carbon increasingly vulnerable to loss (Crowther and Bradford, 2013; MacDougall et al., 2016; Burke et al., 2017; Varney et al., 2020). Significant amounts of soil organic carbon (SOC)

40 would be decomposed and released into the atmosphere from the northern high-latitude thawing permafrost (Field and Raupach, 2004), increasing the atmospheric CO_2 concentrations and activating positive permafrost carbon feedback to accelerate climate warming (Koven et al., 2011; MacDougall et al., 2012).

The degradation of northern high-latitude permafrost has been widely studied using climate models. According to an earlier study, under a high greenhouse gas emission scenario, only 1 million km^2 of near-surface permafrost will remain by

45 2100 (Lawrence and Slater, 2005). The CMIP5 (the Coupled Model Intercomparison Project Phase 5, Taylor et al., 2012) climate models show a linear relationship between the permafrost extent and near-surface air temperature over the observed continuous and discontinuous permafrost region, with an average loss of 1.67 million km^2 in permafrost area under one degree of warming (Slater and Lawrence, 2013). With increased climate sensitivity (Zelinka et al., 2020; Meehl et al., 2020) and warmer climate projections (Wyser et al., 2020), the CMIP6 (Coupled Model Intercomparison Project Phase 6, Eyring et al.,

50 2016) models project a loss of permafrost area between 3.1 and 3.8 million km^2 (25th and 75th percentiles) and a decrease of annual mean frozen volume in the top 2 m soil between 10 % and 40 % per degree of global mean annual surface air temperature increase (Burke et al., 2020). Simulations using the land surface model JSBACH show that, compared to 2005, the frozen carbon in permafrost region at 2100 is reduced by 193 Pg C and 387 Pg C, respectively, under representative concentration pathway 4.5 (rcp45) and 8.5 (rcp85) scenarios (Kleinen and Brovkin, 2018). While an analysis of ensemble simulations from

55 five land surface models shows no significant net losses of permafrost soil carbon before 2100 under both rcp45 and rcp85 scenarios, permafrost in northern high latitudes would likely act as a net carbon source to the atmosphere after this century under rcp85, when soil carbon release could not be compensated by vegetation production (McGuire et al., 2018). The substantial degradation of near-surface permafrost under the rcp85 scenario would lead to an additional warming of around 0.1 °C by 2100 and 0.38 °C by 2200, according to large ensemble simulations performed by a reduced complexity carbon-

60 cycle climate model (Deimling et al., 2012).

Geoengineering is considered as a theoretical option to offset the radiative forcing by anthropogenic factors in addition to mitigation measures. Solar geoengineering as an efficient geoengineering option is designed to mitigate global temperature and reduce some of the associated climate change by deflecting incoming solar radiation back to space and therefore altering the earth's radiative energy budget (Crutzen 2006; Kravitz et al., 2013a; Zhang et al., 2015; Fawzy et al., 2020). Solar

65 geoengineering has often been simulated by reducing the solar constant (known as solar dimming) or by stratospheric aerosol

injection (SAI), and experiments designed for implementation in many climate models have been designed (Kravitz et al.,

2011). The SAI changes the physical climate system and atmospheric chemistry, and presents an impact on the terrestrial

ecosystem and the carbon cycle (Muri et al., 2015; Cao, 2018; Plazzotta et al. 2019; Lee et al., 2021). SAI geoengineering can

enhance terrestrial photosynthesis by changing the ratio of direct to diffuse sunlight (Xia et al., 2016). In an SAI geoengineering

70 simulation with an rcp85 greenhouse gas emissions scenario based on linearly increasing the stratospheric mass ratio of SO_4

with the NorESM1-ME model, soil carbon storage slightly increases due to stabilized surface temperature and reduction in

heterotrophic respiration rate (Tjiputra et al., 2016). Enhanced CO_2 fertilization under geoengineered climate also exerts

considerable impacts on the carbon cycle compared to a climate of the same warming level without geoengineering (Plazzotta

et al. 2019; Lee et al., 2021). In a solar dimming geoengineering plus aggressive mitigation simulated with an earth system

75 model of intermediate complexity, the terrestrial biosphere sequestered more atmospheric CO_2 by 2100 via enhancement of

tropical net primary production with greater accumulation in global total vegetation and soil carbon pools, this carbon feedback

also affects the solar dimming needed (Cao and Jiang, 2017).

The high-latitude permafrost region and its potential carbon feedback under solar geoengineering have been rarely studied.

Lee et al. (2019) studied the responses of the northern high-latitude permafrost and ecosystem under SAI geoengineering

80 scenarios with NorESM1-ME, and found that SAI geoengineering can slow down the permafrost degradation and the

ecosystem is affected by both the inhibited warming and enhanced CO_2 fertilization. Lee et al. (2019) also note that the

permafrost extent and soil temperature would rebound back to ungeoengineered states in two decades following the termination

of SAI geoengineering. Chen et al. (2020) used the soil temperature and net primary production simulated by several earth

system models (ESMs) to drive the Permafrost Carbon Network Incubation–Panarctic Thermal scaling model (PInc-PanTher,

85 Koven et al., 2015) under the Geoengineering Model Intercomparison Project (GeoMIP) G4 scenario which uses rcp45

emissions with SAI geoengineering experiment. They found the permafrost carbon released as CO_2 is halved and as CH_4 is

reduced by 40% compared to the rcp45 experiment. The approaches used above make some simplifications, or even exclude

completely, permafrost physics and carbon dynamics, such as the cryoturbation effects on permafrost carbon vertical mixing

and accumulation (Koven et al., 2009, 2011). The PInc-PanTher approach assumes that soil carbon stocks do not decompose

90 when frozen, but once thawed the soil carbon stocks follow predefined decomposition trajectories as a function of soil

temperature, this simplified approach neglects many important permafrost processes (Koven et al., 2015). An indirect estimate

of reduction in permafrost carbon loss ranged from 27 to 122 Pg C for rcp85 emissions with solar geoengineering maintaining

constant 21st century radiative forcing (Keith et al., 2017).

Different solar geoengineering strategies would exert different impacts on regional climate conditions (Kravitz et al.,

95 2016) and might drive the northern high-latitude permafrost ecosystem response differently (Lee et al., 2019, 2021). Solar

dimming geoengineering produces uneven patterns of significant cooling, with the polar regions being warmer and the tropics

being cooler compared to pure greenhouse gas scenarios of same level radiative forcing (Kravitz et al., 2013a; Yu et al., 2015; Russotto and Ackerman, 2018; Visioni et al., 2021). Similarly equatorial SAI schemes in which sulphate aerosols or their precursors were injected in the equatorial stratosphere, also tend to exhibit higher polar mean annual temperature (Muri et al.,

100   2018; Visioni et al., 2021), the so-called residual polar warming (Henry and Merlis, 2020). The residual polar warming under solar geoengineering has been mainly attributed to seasonal differences in radiative forcing, shortwave reductions can only occur when the sun is above the horizon, whereas as longwave greenhouse gas forcing occurs year-round. Whether the residual polar warming affects the efficacy of solar geoengineering on slowing down permafrost degradation has not been studied. Given very limited existing studies and associated large uncertainty, the response of the northern high-latitude permafrost

105   under solar geoengineering deserves further investigation. Additionally, given the climate model differences in dealing with stratospheric aerosols and their chemistry, using a multi-model approach helps quantify the uncertainties associated with the response.

In this study, we investigate the response of the northern high-latitude permafrost ecosystem under solar geoengineering experiments using multiple models. Our study is organized as follows: In section 2, the observation based dataset, model

110   simulations and methods are presented. In section 3, we present the responses of northern high-latitude permafrost and terrestrial carbon to solar geoengineering. Section 4 is discussion and conclusions.

2 Data and methods

We examine the permafrost extent and terrestrial carbon fluxes and stocks simulated by all five of the CMIP6 earth system models (ESMs) participating in the Geoengineering Model Intercomparison Project (GeoMIP) that have carried out the

115   G6solar and G6sulfur scenarios, and compare with results from the ssp245 and ssp585 scenarios. G6solar reduces radiative forcing from a high-tier emission scenario (Shared Socioeconomic Pathway; ssp585; Meinshausen et al., 2020) to a medium-tier emission scenario (ssp245) levels with uniform reduction in solar constant, whereas G6sulfur through stratospheric aerosol injection from 10°S to 10°N along a single longitude band (Kravitz et al., 2015). The simulated permafrost extent and SOC during the baseline period (1995-2014) are compared with the International Permafrost Association (IPA) permafrost map

120   (Brown et al., 1997) and Northern Circumpolar Soil Carbon Database version 2 (NCSCDv2) (Hugelius et al., 2013, 2014) datasets. Changes in permafrost extent and area, active layer thickness (ALT), carbon fluxes and carbon stocks over the permafrost region under the four scenarios at the end period of this century (2080-2099) relative to the baseline period are analyzed. The multi-model response is reported as the ensemble mean and one standard error.

2.1 Observation based datasets

125   The NCSCDv2 provides estimated storage of SOC in the northern circumpolar permafrost region identified by the IPA permafrost map. The dataset aggregates pedons from regional soil maps homogenized to the U.S. Soil Taxonomy, allowing

SOC storage to be calculated. In pedons where the dataset is incomplete, gap-filling was used to complete calculations over the whole IPA permafrost map. The soil organic carbon content (SOCC) (units of kg C m^{-2}) over the northern circumpolar permafrost region from NCSCDv2 is available at four soil layers: 0-30 cm, 0-100 cm, 100-200 cm and 200-300 cm depth, and

130   at a horizontal resolution of 0.5° × 0.5° is used in this study.

2.2 Model simulations

The five CMIP6 ESMs used in this study are: CESM2-WACCM, UKESM1-0-LL, CNRM-ESM2-1, IPSL-CM6A-LR and MPI-ESM1-2-LR (Table 1). We downloaded monthly data of surface air temperature (tas), precipitation rate (pr), surface downwelling shortwave radiation (rsds), surface upwelling shortwave radiation (rsus), soil temperature (tsl), terrestrial carbon

135   pool (cLand), soil organic carbon pool (cSoil), vegetation carbon pool (cVeg), litter carbon pool (cLitter, not available for UKESM1-0-LL), coarse wood debris pool (cCwd, only available for CESM2-WACCM), gross primary production (gpp), net primary production (npp), heterotrophic respiration (rh) and net ecosystem production (nep, not available for UKESM1-0-LL) from G6solar and G6sulfur simulations along with their historical, ssp245 and ssp585 simulations. All ensemble members of each experiment are averaged for each model and bilinearly regridded to a common resolution of 0.5° × 0.5°. The five models

140   used for analysis have varying representations of terrestrial carbon pools, and we use the relevant combination as shown in Table 1. The net ecosystem production has not been published online for UKESM1-0-LL and is calculated by subtracting heterotrophic respiration from net primary production.

2.3 Deriving permafrost extent and ALT

Two different methods are used to derive permafrost extent. First, we follow the procedures detailed in Chadburn et al.

145   (2017) to derive the probability of permafrost in northern high-latitude by ensemble-mean surface air temperature for each experiment of each model based on an observation-based mean annual air temperature (MAAT)-permafrost probability relationship, which updated an earlier work by Gruber (2012). In this approach, the probability of permafrost is a cumulative normal distribution function of MAAT at each grid cell: $F_{MAAT} = \frac{1}{2} erfc \left(\frac{MAAT+\mu}{\sqrt{2\sigma^2}} \right)$, with mean μ=-4.38°C and standard derivation σ=2.59°C (Chadburn et al., 2017). All grid cells with the probability of finding permafrost ≥ 0.01 are considered as

150   permafrost regions, those with the probability ≥ 0.5 are considered as continuous and discontinuous permafrost, while those with the probability < 0.5 are considered as sporadic and isolated permafrost patches. This approach is also used by Burke et al. (2020) in evaluating permafrost physics in the CMIP6 models and their sensitivity to climate change. Following Burke et al. (2020), the permafrost area is defined as the area of grid cells with the permafrost probability ≥ 0.01, the permafrost extent is defined as the area of grid cells weighted by the permafrost probability in each grid cell. The PF$_{50\%}$ area, on the other hand,

155   is the area of the grid cells where the probability of finding permafrost is ≥ 0.5 and it is not weighted by the proportion of permafrost. To facilitate analysis, we choose the five models' ensemble mean PF$_{50\%}$ region during the baseline period (1995-

2014) as a common region to compare the surface climate, terrestrial carbon fluxes and carbon stocks among different scenarios. This baseline $PF_{50\%}$ region is determined by firstly calculating permafrost probability for each grid cell for each model during the baseline period, then calculating the multi-model ensemble mean permafrost probability and deriving the area of all grid cells with multi-model ensemble mean permafrost probability ≥ 0.5.

160

The second method identifies the existence of permafrost as those grid cells in which the annual maximum monthly ALT is less than 3 m. This method and its variations have been widely used in permafrost studies (e.g. Dankers et al., 2011; Lawrence et al., 2012; Peng et al., 2016; Andresen et al., 2020). To derive ALT for each simulation, the monthly soil temperature was linearly interpolated along the soil depth within the upper 3 m, the maximum depth throughout the year where the soil temperature crosses 0 °C is defined as ALT (Lawrence et al., 2012). For the baseline period and the end period of this century, we use the 20-year averaged monthly soil temperature to diagnose the averaged ALT and the permafrost extent. In the five models, UKESM1-0-LL has a shallow soil column of 3 m depth with the node depth of its lowest soil layer of 2 m, IPSL-CM6A-LR simulates much warmer soil temperature and therefore much smaller permafrost extent during the baseline period possibly due to not accounting for the latent heat release/consumption associated with water freezing/thawing (Boucher et al., 2020; Table 1), therefore these two models were excluded in the analysis based on ALT. The peripheral permafrost area around Greenland is small and its land types are represented inconsistently in climate models, therefore we exclude the Greenland permafrost.

165

170

3 Results

3.1 Changes in surface climate

175

Solar geoengineering is designed to reduce shortwave radiation at the land surface. However, over the baseline $PF_{50\%}$ region at the end period of this century (2080-2099), all four scenarios show increases in surface absorbed solar radiation (R_N) in summer relative to the baseline period (1995-2014) due to reduced surface albedo under the warmer climate, while in winter only minor changes occur due to the lack of solar insolation (not shown). The largest increase in R_N under ssp585 with respect to ssp245 at the end period of this century is mainly due to the largest snow extent retreat among the four scenarios in summer

180

(Figure 1a). G6solar shows similar changes in R_N seasonal cycle as that of ssp245, but G6sulfur shows a decrease in R_N. The spatial pattern of R_N shows an almost uniform decrease under G6sulfur relative to ssp245 in summer at the end period of this century (Figure 1c), which is not the case for G6solar (Figure 1b). R_N is a primary component of the surface energy budget and a fundamental force driving the exchanges of energy, water and carbon between land and the atmosphere (Sellers et al., 1997). The different seasonality change in R_N indicates the surface climate would be different for G6solar and G6suflur.

185

The annual mean surface air warming over the baseline $PF_{50\%}$ region is about twice the mean global warming by the end period of this century, but the annual mean surface air temperature is still well below 0 °C under G6solar, G6sulfur and ssp245

scenarios, and rises above the freezing point under the ssp585 scenario (0.5±0.8 ℃), when the permafrost thaws nearly completely. In all models the G6solar and G6sulfur reduce global mean annual surface air temperature to within 0.2 ℃ of ssp245 levels (Visioni et al., 2021). However, G6solar and G6sulfur show a large residual warming pattern over the high-

190   latitude permafrost region with respect to ssp245 (Figure 1d), especially in the winter over northern Eurasia where G6solar shows year-round residual warming (0.6±0.1 ℃ for winter, 0.5±0.1 ℃ for summer), while under G6sulfur there is stronger seasonality in the year-round residual warming (2.1±0.4 ℃ for winter, 0.2±0.2 ℃ for summer). The relatively warmer summer across the baseline $PF_{50\%}$ region under G6solar relative to ssp245 is a robust feature among the five CMIP6 ESMs (Figure 1e).

G6sulfur shows a greater 2 m soil warming than G6solar with respect to ssp245 in the end period of this century, especially

195   over the northern Eurasia permafrost region. The 2 m soil temperature in the baseline $PF_{50\%}$ region over northern Eurasia has 0.2±0.1 and 0.8±0.4 ℃ residual warming in winter, 0.3±0.1 and 0.6±0.3 ℃ residual warming in summer, respectively under G6solar and G6sulfur relative to ssp245. The residual winter warming in near-surface air temperature will affect the summer permafrost thawing (Burn and Zhang, 2010), and which can be seen by the residual warming in 2 m soil being larger under G6sulfur than G6solar in summer (Figure 1h-i), although it seems quite the opposite of the near-surface air temperature, in

200   which the resisual warming in near-surface air temperature being larger under G6solar than G6sulfur in summer (Figure 1e-f).

Precipitation under solar geoengineering is lower than pure greenhouse gas scenarios of the same warming level due to atmospheric heating imbalance (Niemeier et al., 2013; Kravitz et al., 2013b), enhanced atmospheric stability (Ferraro et al., 2014) and weaker hydrological cycle (Bala et al., 2010; Schmidt et al., 2012; Tilmes et al., 2013; Simpson et al., 2019), and this holds over the northern high-latitude permafrost region as well. G6solar shows similar precipitation changes as ssp245

205   during the non-summer seasons, G6sulfur shows a relatively small increase in precipitation relative to ssp245 during the non-summer seasons, but the precipitation clearly decreases in both G6solar and G6sulfur relative to ssp245 during summer (Figure 1j-l), when the incoming solar radiation has maximum reductions. The reduction in summer total precipitation is 14.6±3.7 mm for G6solar and 18.7±5.0 mm for G6sulfur relative to ssp245 over the baseline $PF_{50\%}$ region, and it is robust among the five earth system models (Figure 1k-l). The larger precipitation reduction in G6sulfur than G6solar can be ascribed to larger R_N

210   reduction in G6sulfur (Figure 1a), as the absorption of longwave radiation by the sulfate aerosols requires a stronger reduction of net downward shortwave surface fluxes than in the case of G6solar, and enhances atmospheric heating imbalance (Niemeier et al., 2013).

3.2 Changes in permafrost extent and ALT

The estimated permafrost extent (permafrost area weighted by permafrost probability in each grid cell) derived from the

215   five earth system models simulated surface air temperature (using 1960-1990 period) is in the range of 12.1-17.5 million km^2 (multi-model ensemble mean: 13.9 million km^2), which is comparable to the 12.0-18.2 million km^2 (mean: 15.5 million km^2) from the reconstructed permafrost map for the same period (Chadburn et al., 2017) and the actual area underlain by permafrost

(12.21 to 16.98 million km^2, Zhang et al., 2000). The baseline permafrost area for the period of 1995-2014 is in the range of 11.0-15.5 million km^2 (multi-model ensemble mean: 12.3 million km^2), covering all permafrost zones in the IPA permafrost

220   map and extending further south (Figure 2a). Our results agree well with existing studies, such as the permafrost area of 15.1±2.6 million km^2 for the period 2000-2014 (Aalto et al., 2018) and 13.9 million km^2 for the period 2000-2016 (Obu et al., 2019). The baseline permafrost of more than 50% probability, the baseline PF$_{50\%}$ region (corresponding to MAAT < -4.38 °C) all locates within the IPA permafrost map with a total area of 12.3 million km^2.

The residual warming over high-latitude permafrost region under G6solar and G6sulfur relative to ssp245 generates some

225   disparities in the permafrost distribution. For the high warming scenario ssp585, the majority of permafrost will thaw by the end period of this century (Burke et al., 2020), with a remnant area of only 1.4 million km^2 that is mostly as sporadic and isolated patches (1.2 million km^2, Figure 2c). For G6solar, G6sulfur and ssp245, however, about 41%, 39% and 45% of the baseline permafrost is preserved respectively (5.0, 4.8 and 5.5 million km^2 for G6solar, G6sulfur and ssp245 respectively), in which the majority is maintained as continuous and discontinuous permafrost, with areas of 3.1, 2.9 and 3.5 million km^2

230   respectively. The modest losses of continuous and discontinuous permafrost zones in G6solar and G6sulfur relative to ssp245 mainly appear at the southern edge, central Canada and Central Siberian Highlands (Figure 2b, d, e). The area of sporadic and isolated patches under G6solar, G6sulfur and ssp245 shows little differences (1.9, 1.9 and 2.0 million km^2 for G6solar, G6sulfur and ssp245 respectively), as they could be transformed from continuous and discontinuous permafrost under a warmer climate.

The existence of surface permafrost is also diagnosed according to whether the annual maximum monthly ALT exceeds

235   3 m for CESM2-WACCM, CNRM-ESM2-1 and MPI-ESM1-2-LR. Baseline permafrost area diagnosed by the ALT method shows a large spread among the three models: CESM2-WACCM (9.6 million km^2, black curve in Figure 3a, b) and CNRM-ESM2-1 (14.9 million km^2, black curve in Figure 3c, d) show a permafrost area comparable with the IPA permafrost map, MPI-ESM1-2-LR (6.8 million km^2, black curve in Figure 3e, f) shows a considerably smaller permafrost region enclosed in the IPA map. Despite the considerable spread in the baseline permafrost area, an unanimously intensive thawing of permafrost

240   is projected for all three models under ssp585 scenario with 91.3-99.3% of the baseline permafrost disappearing due to rapid warming of top 3 m soil by the end period of this century. By contrast, much large proportion of permafrost remains under G6solar, G6sulfur and ssp245, 20.5-31.2%, 11.3-27.1% and 32.1-47.2% of baseline permafrost respectively, which is consistent with the permafrost extent change diagnosed with the observational relationship between MAAT and permafrost probability. CESM2-WACCM shows very similar permafrost extent and relatively smaller differences in ALT under G6solar,

245   G6sulfur and ssp245, especially over Eurasia under G6sulfur, which is due to it having least residual warming with respect to ssp245 over this region among five models (Visioni et al., 2020). CNRM-ESM2-1 and MPI-ESM1-2-LR under G6solar and G6sulfur all show more permafrost losses occurring in the warmer south edges compared to ssp245.

The ALT is generally deeper under G6solar and G6sulfur than ssp245 across much of northern Eurasia despite their spatial patterns of permafrost region being similar (Figure 3). In CESM2-WACCM, ALT over Eurasia tends to be deeper under

250 G6solar than that under ssp245, while over northern Canada its tends to be shallower under G6sulfur (Figure 3a, b). In CNRM-ESM2-1 the average ALT over Eurasia is 0.04 m and 0.18 m deeper under G6solar and G6sulfur respectively than under ssp245 (Figure 3c, d). In contrast for MPI-ESM1-2-LR, the permafrost extent under G6solar and G6sulfur is significantly smaller than ssp245, and the average ALT over northern Eurasia is 0.27 m and 0.37 m deeper than ssp245 (Figure 3e, f). The thicker active layer over northern Eurasia under G6sulfur than G6solar is consistent with warmer 2 m soil temperatures under G6sulfur,

255 although it seems quite the opposite of the near-surface air temperature in summer (Figure 1e-f). Thus, the permafrost extents diagnosed by two different methods confirms that G6solar and G6sulfur can preserve much more high-latitude permafrost than ssp585, but the permafrost area under G6solar and G6sulfur is less than that under ssp245 due to the widespread warmer soil temperature and thicker active layer over northern Eurasia under G6solar and G6sulfur.

3.3 Changes in terrestrial carbon fluxes and carbon stocks

260 #### 3.3.1 Terrestrial carbon fluxes

Changes in temperature and CO_2 fertilization effect would alter the terrestrial carbon cycle. In the baseline $PF_{50\%}$ region, the modeled NPP follows a unified upward trend for the four scenarios during this century as climate warms (Figure 4a). Compared with the baseline period over the $PF_{50\%}$ region, the projected multi-model mean NPP increases by 2.0±0.4, 1.9±0.4, 1.5±0.2 and 2.5±0.4 Pg C yr^{-1} for G6solar, G6sulfur, ssp245 and ssp585 respectively at the end period of this century. Warmer

265 climate over the permafrost region under ssp585 scenario alleviates the temperature limits on high-latitude ecosystem, and results in larger increases in NPP. Surface cooling by implementing G6solar and G6sulfur geoengineering suppresses plant growth at high latitudes relative to ssp585, and the increasing rates in NPP are slower under G6solar and G6sulfur than that for ssp585, although the three scenarios share the same atmospheric CO_2 concentration. NPP seasonal cycle differences among the four scenarios mainly occur from the start of the growing season (April) to late autumn (October) (Figure 4b). Differences

270 in NPP under G6solar and G6sulfur relative to ssp245 peak in June, the relatively larger NPP in G6solar than that of G6sulfur is consistent with warmer temperature and more absorbed surface shortwave radiation under G6solar during summer. G6solar and G6sulfur growth start later in spring than with ssp585 and ends earlier in autumn, which is in line with an earlier study concluding that the reductions in plant primary production at high latitudes under solar geoengineering scenarios were mainly attributable to the shorter growth season (Duan et al., 2020). Therefore, the higher level of atmospheric CO_2 and the warmer

275 climate under G6solar and G6sulfur than for ssp245 enhance plant photosynthesis and primary production, even though soil tends to be slightly drier as precipitation is reduced during summer under G6solar and G6sulfur, indicating that temperature and CO_2 fertilization at high-latitudes play more important roles than soil moisture in plant carbon uptake.

Soil carbon heterotrophic respiration (Rh) in the baseline $PF_{50\%}$ region rises in all scenarios because of warmer soil temperatures (Figure 4c). Compared with the baseline period, multi-model ensemble mean Rh increases by 1.6±0.3, 1.6±0.3,

280 1.4±0.2 and 2.3±0.3 Pg C yr^{-1} at the end period of this century for G6solar, G6sulfur, ssp245 and ssp585 respectively. Warmer

winter soil temperature over the high-latitude permafrost region under G6solar and G6sulfur relative to ssp245 does not significantly accelerate soil carbon decomposition during winter because the soil is well frozen which effectively inhibits microbial activities (Figure 4d). In other seasons, soil carbon decomposition increases under G6solar and G6sulfur relative to ssp245, and Rh increases more in G6solar during summer. The increases in Rh during summer is not only due to warmer

285 summer temperature accelerating microbial activity, but also due to deeper ALT turning more previously frozen SOC to unfrozen states under a warmer decomposition environment. Compared with G6solar and G6sulfur, there is a significant Rh increase in winter under ssp585 at the end period of this century as most of the soil over the baseline $PF_{50\%}$ region does not refreeze due to heating from the deep layer. The increases in Rh during spring, summer and autumn are more profound under ssp585 than G6solar and G6sulfur, showing the significant alleviating effects of G6solar and G6sulfur on permafrost carbon

290 decomposition.

The net ecosystem production (NEP) changes over the baseline $PF_{50\%}$ region are more complex than NPP and Rh. The multi-model ensemble mean NEP suggests that the northern permafrost region is a carbon sink under G6solar, G6sulfur, ssp245 and ssp585 scenarios throughout this century (Figure 4e), but the ability of carbon uptake for ssp245 and ssp585 declines around the middle of this century, while for G6solar and G6sulfur the decline of carbon uptake is delayed until the 2080s.

295 Intensified carbon uptakes under G6solar, G6sulfur and ssp585 relative to ssp245 can be attributed to enhanced carbon uptake in plants during the growing season. The relatively larger carbon uptake under G6solar and G6sulfur than under ssp585 at the end period of this century is due to enhanced CO_2 fertilization being less counteracted by increased soil heterotrophic respiration under G6solar and G6sulfur in summer (Figure 4d), and the permafrost region behaves as a stronger carbon source during cold season under ssp585, weakening its carbon uptake. The increases in NEP suggest that the permafrost ecosystem

300 will still serve as a sink for atmospheric CO_2 for this century, but the decreases in NEP in the middle to late century suggest a lower carbon sequestration capacity, that may become a carbon source in the future even under moderate mitigation or geoengineering implementations. Individual models disagree on the timing of the northern permafrost region switch from carbon sink to carbon source, for example, CESM2-WACCM shows that the permafrost region under ssp585 becomes a carbon source around the middle of 2070s. Overall, the differences in the seasonal cycle of NEP between G6solar, G6sulfur and ssp245

305 follow the differences in NPP and Rh. Non-uniform seasonally residual warming in G6sulfur and G6solar impact terrestrial carbon fluxes almost only in summer and nearly no effects in winter.

The spatial patterns of changes in NPP, Rh and NEP under G6solar and G6sulfur relative to ssp245 during summer by the end period of this century (Figure 5) resemble the changes in near-surface air temperature (Figure 1e-f). Larger changes in NPP, Rh and NEP in the permafrost region under G6solar and G6sulfur relative to ssp245 occur at more southerly latitudes,

310 with smaller changes at higher latitudes. The uncentered pattern correlation between changes in NPP and surface air temperature is 0.95 for G6solar, and 0.35 for G6sulfur. Correspondingly, the uncentered pattern correlation between changes in Rh and surface air temperature is 0.92 for G6solar, and 0.39 for G6sulfur. The uncentered pattern correlation between

changes in NEP and surface air temperature is 0.90 for G6solar, and 0.22 for G6sulfur. The pattern correlation between changes in surface carbon fluxes and surface air temperature are consistently higher for G6solar than that for G6sulfur, this might be

315   due to relatively larger changes in surface air temperature (Figure 1e-f) and surface carbon fluxes (Figure 5) during summer under G6solar than that under G6sulfur relative to ssp245, hence relatively larger signal-to-noise ratios manifested as higher spatial pattern correlations. The above results indicate residual warming in summer plays an important role in differential responses of high-latitude permafrost ecosystem under G6solar and G6sulfur relative to ssp245.

3.3.2 Terrestrial carbon stocks

320   The enhanced plant photosynthesis under high atmospheric CO_2 concentration and warmer climate results in gains in vegetation carbon over the permafrost region (Figure 6). As with NPP, the projections of vegetation carbon accumulation in the baseline $PF_{50\%}$ region until the end period of this century are 15.7±2.6, 15.2±2.4, 13.5±2.0 and 18.7±2.8 Pg C for G6solar, G6sulfur, ssp245 and ssp585. Except for IPSL-CM6A-LR under G6sulfur, all models show that vegetation carbon gains under G6solar and G6sulfur are greater than that under ssp245. IPSL-CM6A-LR shows a smaller NPP for G6sulfur than ssp245 from

325   the 2070s and this slows down the gains in vegetation carbon under G6sulfur, with 0.6 Pg C less than that for ssp245 at the end period of this century. The litter carbon pool is expected to increase as the vegetation carbon increases. Four of the five earth system models (CESM2-WACCM, CNRM-ESM2-1, IPSL-CM6A-LR and MPI-ESM1-2-LR) have litter carbon pools available, and show increases of 8.2±3.9, 7.4±3.6, 5.9±2.2 and 6.5±3.0 Pg C for G6solar, G6sulfur, ssp245 and ssp585 scenarios respectively. Gains in litter carbon pool have direct impacts on soil carbon inputs, along with enhanced soil

330   decomposition rates under warmer soil temperatures.

The total SOC increases more under G6solar and G6sulfur than that under ssp245 and ssp585 scenarios over the permafrost region (Figure 6). It is projected that multi-model ensemble mean total SOC over the baseline $PF_{50\%}$ region increases by 17.7±8.0, 16.4±7.5, 13.6±5.7 and 13.0±8.0 Pg C for G6solar, G6sulfer, ssp245 and ssp585, respectively. The slower accumulation in SOC under ssp585 is mainly due to enhanced soil carbon decomposition under much warmer

335   temperatures compared with the other three scenarios. There is a large spread in the baseline permafrost SOC amount among the five earth system models, which affects the SOC available to participate in microbial decomposition under warmer conditions (Chen et al., 2020). In the five models, only CESM2-WACCM simulates a baseline permafrost SOC of 847.3 Pg C that is comparable to the observational estimate of 1091.3 Pg C according to the NCSCDv2 dataset. However, CESM2-WACCM projects net loss in SOC by 1.3, 0.8, 2.8 and 11.7 Pg C during this century for G6solar, G6sulfur, ssp245 and ssp585,

340   respectively, as a result of its large baseline SOC stock and rapid soil carbon decomposition under warming. The other four models all project gains in permafrost SOC under the four scenarios.

The vegetation carbon increases faster under G6solar and G6sulfur than ssp245 but slower than ssp585 over the permafrost region as G6solar and G6sulfur have stronger CO_2 fertilization effects than ssp245 and are cooler than ssp585, as

evidenced by the differences in the accumulated NPP (Figure 6). However, soil carbon increases faster under G6solar and

345   G6sulfur than both ssp245 and ssp585 over the permafrost region as G6solar and G6sulfur have more vegetation carbon available to transfer to soil carbon than ssp245 and less soil carbon decomposition than ssp585 as evidenced by the differences in the accumulated Rh (Figure 6). The vegetation carbon uptake and soil carbon decomposition moderate the changes of terrestrial carbon pools under future scenarios.

All models consistently project increases in permafrost terrestrial carbon under the four scenarios (Figure 6), with multi-

350   model average gains in terrestrial carbon of 32.2 ± 10.0, 30.6 ± 9.5, 26.1 ± 6.8 and 30.8 ± 9.6 Pg C at the end period of this century for G6solar, G6sulfur, ssp245 and ssp585 respectively, in the baseline $PF_{50\%}$ region. For CESM2-WACCM, although it projects net loss in SOC during this century for all the four scenarios, gains in vegetation carbon over the baseline $PF_{50\%}$ region compensates for soil carbon loss due to enhanced soil carbon decomposition, and terrestrial carbon increases by 10.7, 10.4, 8.1 and 5.0 Pg C at the end period of this century for G6solar, G6sulfur, ssp245 and ssp585 respectively. The simulations under

355   the four scenarios suggest net losses of permafrost ecosystem carbon would not happen before the end of this century, the enhanced soil carbon decomposition cannot offset increased vegetation carbon uptake, and the northern high-latitude permafrost region is expected to be a small carbon sink, this is consistent with previous estimations from CMIP5 models (Burke et al., 2013) and land model only simulations (McGuire et al., 2018).

3.4 Changes in soil carbon inputs and turnover times

360   Soil carbon inputs are derived from changes in SOC and the organic carbon that is decomposed. The collective increases in NPP lead to soil carbon inputs growth under all four scenarios (Figure 7a). In the baseline $PF_{50\%}$ region, the increase in annual soil carbon inputs during this century is most remarkable for ssp585 (2.2 ± 0.3 PgC·yr^{-1}), then 1.8 ± 0.4 PgC·yr^{-1} for G6solar and 1.7 ± 0.4 PgC·yr^{-1} for G6sulfur. ssp245 has the lowest CO_2 fertilization effect and the smallest growth in NPP so its increases in permafrost soil carbon inputs (1.4 ± 0.2 PgC·yr^{-1}) is also the smallest among the four scenarios. Annual soil

365   carbon inputs in the baseline $PF_{50\%}$ region vary considerably among the models with the smallest amounts in IPSL-CM6A-LR (3.2, 2.8, 3.1 and 3.4 PgC·yr^{-1} under G6solar, G6sulfur, ssp245 and ssp585 respectively) and the largest amounts in CNRM-ESM2-1 (6.6, 6.6, 5.4 and 6.8 PgC·yr^{-1} under G6solar, G6sulfur, ssp245 and ssp585 respectively) at the end period of this century. However, the ratio of soil carbon inputs to NPP is similar for all scenarios: $93.1\pm1.0\%$, $93.7\pm0.9\%$, $94.1\pm0.9\%$ and $91.8\pm1.2\%$ of NPP for G6solar, G6sulfur, ssp245 and ssp585, respectively. The majority of annual NPP becomes soil carbon

370   inputs in permafrost area just as it does for global terrestrial NPP in CMIP5 models (Todd-Brown et al., 2014), and G6solar and G6sulfur are relatively more efficient than ssp245 in turning assimilated vegetation carbon to soil carbon. The less efficient conversion of NPP to soil carbon under ssp585 might be due to more frequent wild fires in the warmer climate with more dry ground fuel in degraded permafrost (Krause et al., 2014; Turetsky et al., 2015; Veraverbeke et al., 2017) and four of the five models (except for UKESM1-0-LL) analyzed in this study simulate wild fires.

375   Changes in turnover times arise from both soil carbon input changes from litter-fall related to carbon-concentration feedback, and heterotrophic respiration change associated with carbon-climate feedback. The SOC turnover times are calculated as the ratio of total SOC stock and heterotrophic respiration for each model (Todd-Brown et al., 2014). In the baseline $PF_{50\%}$ region, the models show a wide spread in permafrost SOC turnover times during the baseline period, mainly due to their large differences in the SOC stocks, and poor representation of permafrost SOC dynamics may also lead to

380   inaccurate turnover time (Shu et al., 2020). Of the five models, only CESM2-WACCM explicitly considers vertically heterogeneities in SOC resulting from the cryoturbation process which would slow down SOC decomposition, and CESM2-WACCM simulates a much longer turnover time (336 years) than the other four models (32-108 years) during the baseline period. The decline over this century in permafrost SOC turnover time from CESM2-WACCM is 2.7-13.2 times of the other four models due to stronger heterotrophic respiration in CESM2-WACCM. However, the magnitude of SOC turnover time and

385   its decline of CESM2-WACCM is in line with a land surface model including a detailed description of vertical heterogeneity in permafrost soils (Shu et al., 2020). Despite the large inter-model spread in permafrost SOC turnover times, the relative changes in turnover time are more consistent among models, with declines of 32.0±2.9 %, 31.4±2.8%, 28.9±2.5% and 42.5±3.0% for G6solar, G6sulfur, ssp245 and ssp585 through this century (Figure 7b). The turnover times decrease by 13.7±1.4% for ssp585 relative to ssp245, while only decrease by 3.2±1.1% and 2.5±1.8% for G6solar and G6sulfur relative to

390   ssp245. ssp585 shows the largest increases in soil carbon inputs and largest decreases in turnover time, while ssp245 shows the smallest increase in soil carbon inputs and smallest decrease in turnover time (Figure 7), illustrating that changes in turnover times arise mostly from the heterotrophic respiration change associated with carbon-climate feedback over the permafrost region. This is further confirmed by the fact that the turnover time changes under G6solar and G6sulfur are more like ssp245 (Figure 7b), although G6solar and G6sulfur have soil carbon inputs between ssp245 and ssp585 (Figure 7a).

395   **3.5 Drivers of SOC change**

The fates of permafrost carbon are not quite the same for G6solar and G6sulfur as for ssp585 and ssp245. Increases in soil carbon inputs and decomposition rates oppose each other in changing SOC (Todd-Brown et al., 2014). Soil carbon inputs and decomposition rates show similar increases during this century for all except for the ssp585 scenario. Soil carbon inputs increase by 70.0±9.5%, 65.3±8.5%, 57.2±8.8% and 89.2±8.5%, soil carbon decomposition rates increase by 69.1±10.6%,

400   65.6±8.9%, 58.9±10.0% and 97.1±10.8% for G6solar, G6sulfur, ssp245 and ssp585, respectively. Soil carbon decomposition rates increase faster than that of soil carbon inputs under ssp585. However, because soil carbon inputs are larger than soil carbon decomposition, multi-model ensemble mean permafrost SOC continues increasing throughout this century under the four scenarios. During the period 2015-2099 over the baseline $PF_{50\%}$ region, G6solar and G6sulfur gain 13.9±8.7 and 11.7±9.0 Pg C more soil carbon than ssp245, mostly due to the enhanced CO_2 fertilization, which reinforces plant growth and litter-fall, thus further increasing soil carbon inputs and soil carbon storage. At the same time, G6solar and G6sulfur decompose 8.9±5.1

405

and 8.2±6.2 Pg C more SOC than ssp245, with net gains of 5.0±3.5 and 3.5±3.0 Pg C more SOC than ssp245. In contrast, under the joint action of enhanced CO_2 fertilization effects and more warming, ssp585 gains 30.6±6.5 Pg C more soil carbon inputs and decomposes 32.4±6.1 Pg C more SOC relative to ssp245, with a net accumulation of 1.9±3.2 Pg C less SOC than ssp245.

410   3.6 Changes in thawed permafrost soil carbon

As ALT deepens under warmer climates, more previously frozen SOC becomes vulnerable to decomposition within thawed soil volume, especially during summer when both annual ALT and SOC decomposition rates reach their maximum. The CESM2-WCCM simulation of historical permafrost extent based on annual maximum ALT, and permafrost SOC are both close to the observational estimates. CESM2-WACCM also has a sensitivity of thawed permafrost volume to global MAAT close to the median of CMIP6 models (Burke et al., 2020). Hence, CESM2-WACCM simulated ALT changes can be useful in representing SOC thaw and exposure to accelerated decomposition during summer under the four scenarios. As layered soil carbon mass is not available, we use the total SOC simulated by CESM2-WACCM and the vertical SOC density profile derived from the NCSCDv2 dataset to distribute simulated SOC with soil depth and neglect changes in vertical SOC density profile under warming. Burke et al. (2012, 2013) used a similar approach to diagnose permafrost carbon vulnerable to decomposition per degree of global warming.

As shown in Section 3.2, CESM2-WACCM has a baseline permafrost extent of 9.6 million km^2 where the top 3 m soil is not completely thawed (Figure 3a, b), over this permafrost region during the baseline period, the annual maximum thawed volume and SOC of upper 3 m of soil are $12.0×10^3$ km^3 and 317.5 Pg C, while the total SOC is 766.6 Pg C. Under G6solar, G6sulfur, ssp245 and ssp585, the annual maximum thawed volume increases by $9.6×10^3$, $9.3×10^3$, $9.9×10^3$ and $16.0×10^3$ km^3 respectively, the annual maximum thawed amount of SOC increases by 186.7, 174.5, 189.8 and 406.3 Pg C respectively. Consequently, the proportion of exposed permafrost SOC increases from 41.4% during the baseline period to 65.8%, 64.2%, 66.2% and 94.4% under the combined effects of ALT deepening and soil carbon accumulation. In summer, nearly all permafrost at the top 3m soil would be thawed by the end period of this century under ssp585, with almost all the permafrost SOC unfrozen and exposed to accelerated decomposition conditions, potentially releasing more greenhouse gases to the atmosphere and amplifying climate warming through the permafrost carbon feedback. Conversely, G6solar, G6sulfur and ssp245 preserve more frozen soil and SOC (Figure 8a, b) and alleviate the permafrost carbon feedback, reducing the exposure of permafrost SOC to decomposition. The frozen soil volume and SOC under G6solar and G6sulfur are close to that under ssp245 due to the weak residual warming simulated by CESM2-WACCM, especially for G6sulfur over northern Eurasia (Visioni et al., 2020).

Changes in the exposed permafrost soil carbon depend not only on the varying ALT but also on varying permafrost SOC, their relative importance in modulating annual maximum thawed SOC can be illustrated by fixing ALT at the baseline period and evaluating how the exposed permafrost SOC changes. Figure 8c shows the amount of SOC in the baseline thawed volume

decreases relatively slowly even for ssp585, which reflects the overall trend of SOC simulated by CESM2-WACCM under the four scenarios through this century. Hence, the time-varying permafrost SOC exerts relatively minor impacts on the changes in the thawed SOC. It is ALT deepening that dominates the changes in the amount of thawed SOC under different warming

440   scenarios. As the residual high-latitude warming under G6solar and G6sulfur relative to ssp245 is not large for CESM2-WACCM, the spatial distributions of ALT among G6solar, G6sulfur and ssp245 are close, hence the annual maximum thawed SOC is also similar. For models with larger residual high-latitude warming, such as CNRM-ESM2-1, the annual maximum thawed SOC may be considerably larger under G6solar and G6sulfur than that under ssp245, although still much less than that under ssp585. Therefore, G6solar and G6sulfur alleviate the permafrost carbon feedback mainly by reducing the ALT

445   deepening. If the residual warming over high-latitude permafrost regions is well controlled, solar geoengineering would be more effective in alleviating permafrost carbon feedback.

4 Discussion and conclusions

The soil stores the majority of organic carbon in the terrestrial biosphere with the largest stocks in the northern high-latitude permafrost regions (Hengl et al., 2014), which is widely considered as a non-linear tipping point element in the Earth's

450   climate system (Lenton et al., 2008). How the northern high-latitude permafrost carbon responds in the future has drawn significant attention (Schuur et al., 2015), but its response to solar geoengineering has been rarely studied. This study compares changes in permafrost and terrestrial carbon responses under G6solar and G6sulfur solar geoengineering scenarios with that under ssp245 and ssp585 scenarios.

G6solar and G6sulfur show significant residual warming over the northern high-latitudes relative to ssp245, even though

455   mean global temperatures were changed from ssp585 to ssp245 levels. The residual warming of near-surface air is more profound over northern Eurasia in winter under G6sulfur, and this exerts significant influence on the degradation of permafrost in summer. The winter surface warming at high latitudes under SAI geoengineering has previously been reported by Jiang et al. (2019), Simpson et al. (2019), Banerjee et al. (2021) and Visioni et al. (2021), and it is attributed to seasonal differences in radiative forcing and dynamical effects of injected stratospheric aerosol (Jones et al., 2021). The broad-scale patterns of

460   temperature perturbation over northern Eurasia during boreal winter under SAI resemble those associated with a positive phase of the North Atlantic Oscillation (NAO) observed subsequent to large tropical volcanic eruptions (Shindell et al., 2004; Jones et al., 2021), similar results were found in another SAI experiment manifested as altered seasonal cycles of temperature and snow at northern high latitudes (Jiang et al., 2019). In addition, even without the dynamical effects of SAI, the difference in the vertical structure of temperature change between increasing CO_2, decreasing insolation, and decreasing atmospheric energy

465   transport also produce residual surface warming at northern high latitudes under solar geoengineering (Henry and Merlis, 2020).

Precipitation under solar geoengineering is generally less than that of pure greenhouse gas scenarios with the same warming level (Bala et al., 2010; Schmidt et al., 2012; Niemeier et al., 2013; Tilmes et al., 2013; Ferraro et al., 2014; Simpson et al., 2019), and this also holds over the northern high-latitude permafrost region under G6solar and G6sulfur. G6solar and

470   G6sulfur show mild reductions in summer precipitation relative to ssp245 over the northern high-latitude permafrost region, and similar precipitation as ssp245 in other seasons. The mild reduction in summer precipitation would be expected to only slightly modify surface soil moisture and it is not likely to significantly affect the vegetation growth and environment for SOC decomposition according to the sensitivity analysis for CMIP5 models (Todd-Brown et al., 2013, 2014). Therefore, the main factors affecting the northern high-latitude permafrost ecosystem are the residual warming and enhanced CO_2 fertilization

475   effects (Govindasamy et al., 2002; Glienke et al., 2015) under G6solar and G6sulfur compared with ssp245.

Based on the observationally constructed relationship between MAAT and permafrost probability, the diagnosed multi-model mean permafrost area during the baseline period is 12.3 million km^2. At the end period of this century, only 11% of the baseline permafrost will be preserved under ssp585 and most of them are sporadic and isolated patches being confined to the northernmost part of the Arctic. G6solar, G6sulfur and ssp245 would preserve 41%, 39% and 45% of the baseline permafrost

480   area respectively to the end period of this century. The surviving continuous and discontinuous permafrost under the mitigation and geoengineering scenarios are mostly in central and eastern parts of both northern Canada and northern Siberia. G6solar and G6sulfur have thicker active layer and more unfrozen SOC than ssp245 due to the robust residual high-latitude warming under solar geoengineering. The winter residual warming over northern Eurasia exerts profound effects on permafrost degradation under G6sulfur.

485   G6solar and G6sulfur accumulate more soil carbon than ssp245 and ssp585 over the northern high-latitude permafrost region due to enhanced CO_2 fertilization effects relative to ssp245 and weakened heterotrophic respiration relative to ssp585. The asynchronous changes in CO_2 fertilization effects and heterotrophic respiration, and hence soil carbon inputs and soil carbon decomposition directly result from decoupling of atmospheric CO_2 concentration and temperature under solar geoengineering. The northern high-latitude permafrost region remains as a carbon sink throughout this century under the four

490   scenarios, and the geoengineering scenarios tend to delay the timing of the northern high-latitude permafrost region switching from carbon sink to carbon source in the future. These results are in line with several previous studies, which suggest that with warming and elevated atmospheric CO_2 concentrations, northern high-latitude ecosystems will sequester additional carbon through the end of this century because increases in plant productivity offset accelerated decomposition rates (Koven et al., 2015; McGuire et al., 2018).

495   G6solar and G6sulfur can slow permafrost degradation and protect a large part of permafrost carbon from microbial decomposition compared to ssp585. These results are consistent with Lee et al. (2019), who found that solar geoengineering can slow down permafrost degradation and increase NPP of high-latitude vegetation based on simulations conducted with a single earth system model. However, G6solar and G6sulfur cannot restore the northern high-latitude permafrost system under

ssp585 greenhouse gas concentrations to that under ssp245 due to regional climate variations resulting from the residual high-
latitude warming (Kravitz et al., 2013a; Henry and Merlis, 2020). The decoupling of temperature and atmospheric CO_2
concentration under solar geoengineering means that G6solar and G6sulfur store more SOC than ssp245 and ssp585. If G6solar
and G6sulfur geoengineering were terminated in an uncontrolled way the soil temperature would rebound rather quickly to
ssp585 levels (Lee et al., 2019) triggering rapid permafrost carbon feedback.

The projection of future permafrost degradation not only depends on the model's sensitivity of permafrost volume to
global MAAT (Burker et al., 2020), but also depends on the model's climate sensitivity, simulated Arctic amplification and
many other factors as well. CMIP6 models exhibit a higher transient climate response (Meehl et al., 2020) and effective
equilibrium climate sensitivity than previous generations of climate models (Zelinka et al., 2020). Two of the five models
(IPSL-CM6A-LR and UKESM1-0-LL) used in this study are of high climate sensitivity models (Hausfather et al., 2022),
which can be expected to show relatively larger permafrost degradation under future climate scenarios. The five models used
in this study can reasonably reproduce the historical permafrost extent based on the observational relationship between MAAT
and permafrost probability, but the models could not reconstruct the historical permafrost extent well using simulated soil
temperature, which reflects their divergence in land-atmosphere coupling and defects in biogeophysical and hydrological
parameterizations over cold regions (Wang et al., 2016; Burke et al., 2020). The five models agree on the increasing trends in
NPP, Rh and terrestrial carbon stocks under the four scenarios mainly driven by enhanced CO_2 fertilization effects and warmer
climate. All models except CESM2-WACCM agree on the increasing trends of SOC under the four scenarios, but these four
models largely underestimate the permafrost carbon stocks, which is also a common problem of many CMIP5 and CMIP6
models (Todd-Brown et al., 2013; Ito et al., 2020; Varney et al., 2022). Our results show that future projections of permafrost
soil carbon stock are driven by changes in plant productivity and microbial activity under both geoengineered and pure
greenhouse gas climates, therefore the uncertainties in projected changes over high-latitude permafrost ecosystem can be
attributed to the response of GPP to atmospheric CO_2 fertilization, the modeling of heterotrophic respiration and the fate of
soil carbon in newly thawed permafrost (McGuire et al., 2016).

Despite implications for permafrost carbon feedback under climate warming, most CMIP6 earth system models still have
inadequate representation of permafrost carbon cycle (Melnikova et al., 2020; Varney et al., 2022), which hinders a
comprehensive assessment of permafrost response to solar geoengineering. In the five models analyzed, only CESM2-
WACCM vertically resolves SOC and considers the impacts of cryoturbation mixing on vertical SOC transportation, which
are important processes to accumulate permafrost carbon stock and further affects the magnitude of cumulative carbon
decomposition (Koven et al., 2009; 2010). The current generation of earth system models do not well parameterize the
evolution of mineral-organic interactions with permafrost thaw (Opfergelt, 2020), subgrid processes such as the development
of thermokarst landscapes and lakes (Anthony et al., 2018), interactions between permafrost degradation and fire activities
(Box et al., 2019), and the microbial decomposition of SOC and subsequent CO_2 release in winter (Natali et al., 2019).

Therefore, the complex nature of the northern high-latitude permafrost ecosystem emphasizes the importance of using more detailed earth system models to study the regional impacts of solar geoengineering.

This study analyzes the response of high-latitude permafrost under solar geoengineering, without assessing its feedback on regional or global climate systems. Cao and Jiang (2017) find the carbon cycle-climate feedback raises the amount of

535 required solar geoengineering to reach targeted warming levels without considering the permafrost carbon feedback. How much the permafrost carbon feedback would change the efficiency of solar geoengineering depends on specific warming targets and pathways to reach them (Gasser et al., 2018; Kleinen and Brovkin, 2018), these require specifically designed geoengineering experiments to access and are beyond the current scope of GeoMIP. Earth system models are an indispensable tool to examine the effects of different solar geoengineering methods, but only a few models have conducted the G6solar and

540 G6sulfur experiments, and few studies have focused on the regional carbon cycle responses to solar geoengineering. We encourage more modeling groups to focus on high-latitude and perform the GeoMIP-type experiments.

Data availability

All CMIP6 and GeoMIP simulation data used in this work are available from the Earth System Grid (https://esgf-node.llnl.gov/search/ cmip6/, WCRP, 2022). NCSCD v2 SOC dataset is available from https://bolin.su.se/data/ncscd/

545 (NCSCDv2, 2022).

Author contributions

DJ designed the research. YC performed the analysis and wrote the initial manuscript. DJ, QZ and JCM revised the manuscript. OB, AJ, TL, MJM, UN, RS and ST performed the simulations and offered valuable comments on the manuscript.

Competing interests

550 The authors declare that they have no conflict of interest.

Acknowledgements

We acknowledge the World Climate Research Programme for coordinating and promoting CMIP and all participants of CMIP6 and GeoMIP. We thank the Super Computing Center of Beijing Normal University for providing computing resources. We thank Dr. Burke for providing the computer code calculating permafrost probability with the observation-based relationship.

555 This study was supported by National Nature Science Foundation of China (No. 41875126). Andy Jones was supported by the Met Office Hadley Centre Climate Programme funded by BEIS. Ulrike Niemeier has been supported by the Deutsche Forschungsgemeinschaft Research Unit VollImpact (FOR2820 (grant no. 398006378)) and used resources of the Deutsches

Klimarechenzentrum (DKRZ) granted by its Scientific Steering Committee (WLA) under project ID bm0550. Roland Séférian

acknowledges the European Union's Horizon 2020 research and innovation program under grant agreement No. 101003536

560   (ESM2025 – Earth System Models for the Future) and H2020 CONSTRAIN under the grant agreement No 820829.

References

Aalto, J., Karjalainen, O., Hjort, J., and Luoto, M.: Statistical Forecasting of Current and Future Circum-Arctic Ground

Temperatures and Active Layer Thickness, Geophys. Res. Lett., 45, 4889-4898, https://doi.org/10.1029/2018GL078007,

2018.

565   Andresen, C. G., Lawrence, D. M., Wilson, C. J., McGuire, A. D., Koven, C., Schaefer, K., Jafarov, E., Peng, S., Chen, X.,

Gouttevin, I., Burke, E., Chadburn, S., Ji, D., Chen, G., Hayes, D., and Zhang, W.: Soil moisture and hydrology

projections of the permafrost region - a model intercomparison, The Cryosphere, 14, 445-459, https://doi.org/10.5194/tc-

14-445-2020, 2020.

Anthony, K. W., Schneider Von Deimling, T., Nitze, I., Frolking, S., Emond, A., Daanen, R., Anthony, P., Lindgren, P.,

570   Jones, B., and Grosse, G.: 21st-century modeled permafrost carbon emissions accelerated by abrupt thaw beneath lakes,

Nat. Commun., 9, 1-11, https://doi.org/10.1038/s41467-018-05738-9, 2018.

Bala, G., Caldeira, K., and Nemani, R.: Fast versus slow response in climate change: implications for the global hydrological

cycle, Clim. Dynam., 35, 423-434, https://doi.org/10.1007/s00382-009-0583-y, 2010.

Banerjee, A., Butler, A. H., Polvani, L. M., Robock, A., Simpson, I. R., and Sun, L.: Robust winter warming over Eurasia

575   under stratospheric sulfate geoengineering - the role of stratospheric dynamics, Atmos. Chem. Phys., 21, 6985-6997,

https://doi.org/10.5194/acp-21-6985-2021, 2021.

Biskaborn, B. K., Smith, S. L., Noetzli, J., Matthes, H., Vieira, G., Streletskiy, D. A., Schoeneich, P., Romanovsky, V. E.,

Lewkowicz, A. G., Abramov, A., Allard, M., Boike, J., Cable, W. L., Christiansen, H. H., Delaloye, R., Diekmann, B.,

Drozdov, D., Etzelmüller, B., Grosse, G., Guglielmin, M., Ingeman-Nielsen, T., Isaksen, K., Ishikawa, M., Johansson, M.,

580   Johannsson, H., Joo, A., Kaverin, D., Kholodov, A., Konstantinov, P., Kröger, T., Lambiel, C., Lanckman, J., Luo, D.,

Malkova, G., Meiklejohn, I., Moskalenko, N., Oliva, M., Phillips, M., Ramos, M., Sannel, A. B. K., Sergeev, D., Seybold,

C., Skryabin, P., Vasiliev, A., Wu, Q., Yoshikawa, K., Zheleznyak, M., and Lantuit, H.: Permafrost is warming at a global

scale, Nat. Commun., 10, 1-11, https://doi.org/10.1038/s41467-018-08240-4, 2019.

Bockheim, J. G.: Importance of cryoturbation in redistributing organic carbon in permafrost-affected soils, Soil Sci. Soc.

585   Am. J., 71, 1335-1342, https://doi.org/10.2136/sssaj2006.0414N, 2007.

Boucher, O., Servonnat, J., Albright, A. L., Aumont, O., Balkanski, Y., Bastrikov, V., Bekki, S., Bonnet, R., Bony, S., and

Bopp, L.: Presentation and evaluation of the IPSL-CM6A-LR climate model, J. Adv. Model. Earth Sy., 12,

2019MS002010, https://doi.org/10.1029/2019MS002010, 2020.

Box, J. E., Colgan, W. T., Christensen, T. R., Schmidt, N. M., Lund, M., Parmentier, F. W., Brown, R., Bhatt, U. S.,

590   Euskirchen, E. S., and Romanovsky, V. E.: Key indicators of Arctic climate change: 1971-2017, Environ. Res. Lett., 14,
        045010, https://doi.org/10.1088/1748-9326/aafc1b, 2019.

Brown, J., Ferrians Jr, O. J., Heginbottom, J. A., and Melnikov, E. S.: Circum-arctic map of permafrost and ground ice
        conditions Washington, DC: U.S. Geological Survey in Cooperation with the Circum-Pacific Council for Energy and
        Mineral Resources, Circum-Pacific Map Series CP-45, scale 1:10,000,000, 1 sheet, 1997.

595   Burke, E. J., Ekici, A., Huang, Y., Chadburn, S. E., Huntingford, C., Ciais, P., Friedlingstein, P., Peng, S., and Krinner, G.:
        Quantifying uncertainties of permafrost carbon – climate feedbacks, Biogeosciences, 14, 3051-3066,
        https://doi.org/10.5194/bg-14-3051-2017, 2017.

Burke, E. J., Zhang, Y., and Krinner, G.: Evaluating permafrost physics in the Coupled Model Intercomparison Project 6
        (CMIP6) models and their sensitivity to climate change, The Cryosphere, 14, 3155-3174, https://doi.org/10.5194/tc-14-

600   3155-2020, 2020.

Burn, C. R., and Zhang, Y.: Sensitivity of active-layer development to winter conditions north of treeline, Mackenzie delta
        area, western Arctic coast, in: Proceedings of the 6th Canadian Permafrost Conference, The 63rd Canadian Geotechnical
        Conference, Calgary, Alberta, 12-16 September 2010, http://pubs.aina.ucalgary.ca/cpc/CPC6-1458.pdf, 1458-1465, 2010.

Cao, L., and Jiang, J.: Simulated Effect of Carbon Cycle Feedback on Climate Response to Solar Geoengineering, Geophys.

605   Res. Lett., 44, 12-484, https://doi.org/10.1002/2017GL076546, 2017.

Cao, L.: The Effects of Solar Radiation Management on the Carbon Cycle, Current Climate Change Reports, 4, 41-50,
        https://doi.org/10.1007/s40641-018-0088-z, 2018.

Chadburn, S. E., Burke, E. J., Cox, P. M., Friedlingstein, P., Hugelius, G., and Westermann, S.: An observation-based
        constraint on permafrost loss as a function of global warming, Nat. Clim. Change, 7, 340-344,

610   https://doi.org/10.1038/nclimate3262, 2017.

Chen, Y., Liu, A., and Moore, J. C.: Mitigation of Arctic permafrost carbon loss through stratospheric aerosol
        geoengineering, Nat. Commun., 11, 1-10, https://doi.org/10.1038/s41467-020-16357-8, 2020.

Crowther, T. W., and Bradford, M. A.: Thermal acclimation in widespread heterotrophic soil microbes, Ecol. Lett., 16, 469-
        477, https://doi.org/10.1111/ele.12069, 2013.

615   Crutzen, P. J.: Albedo Enhancement by Stratospheric Sulfur Injections: A Contribution to Resolve a Policy Dilemma?
        Climatic Change, 77, 211, https://doi.org/10.1007/s10584-006-9101-y, 2006.

Dankers, R., Burke, E. J., and Price, J.: Simulation of permafrost and seasonal thaw depth in the JULES land surface scheme,
        The Cryosphere, 5, 773-790, https://doi.org/10.5194/tc-5-773-2011, 2011.

Decharme, B., Delire, C., Minvielle, M., Colin, J., Vergnes, J. P., Alias, A., Saint Martin, D., Séférian, R., Sénési, S., and

620 Voldoire, A.: Recent Changes in the ISBA-CTRIP Land Surface System for Use in the CNRM-CM6 Climate Model and in Global Off-Line Hydrological Applications, J. Adv. Model. Earth Sy., 11, 1207-1252, https://doi.org/10.1029/2018MS001545, 2019.

Delire, C., Séférian, R., Decharme, B., Alkama, R., Calvet, J. C., Carrer, D., Gibelin, A. L., Joetzjer, E., Morel, X., Rocher, M., and Tzanos, D.: The Global Land Carbon Cycle Simulated With ISBA-CTRIP: Improvements Over the Last Decade,

625 J. Adv. Model. Earth Sy., 12, e2019MS001886, https://doi.org/10.1029/2019MS001886, 2020.

Eyring, V., Bony, S., Meehl, G. A., Senior, C. A., Stevens, B., Stouffer, R. J., and Taylor, K. E.: Overview of the Coupled Model Intercomparison Project Phase 6 (CMIP6) experimental design and organization, Geosci. Model Dev., 9, 1937-1958, https://doi.org/10.5194/gmd-9-1937-2016, 2016.

Fawzy, S., Osman, A. I., Doran, J., and Rooney, D. W.: Strategies for mitigation of climate change: a review, Environ.

630 Chem. Lett., 18, 2069-2094, https://doi.org/10.1007/s10311-020-01059-w, 2020.

Ferraro, A. J., Highwood, E. J., and Charlton-Perez, A. J.: Weakened tropical circulation and reduced precipitation in response to geoengineering, Environ. Res. Lett., 9, 014001, https://doi.org/10.1088/1748-9326/9/1/014001, 2014.

Field, C. B., and Raupach, M. R. (Eds.): The global carbon cycle: integrating humans, climate, and the natural world, Island Press, 2004.

635 Gasser, T., Kechiar, M., Ciais, P., Burke, E. J., Kleinen, T., Zhu, D., Huang, Y., Ekici, A., and Obersteiner, M.: Path-dependent reductions in CO_2 emission budgets caused by permafrost carbon release, Nat. Geosci., 11, 830-835, https://doi.org/10.1038/s41561-018-0227-0, 2018.

Gruber, S.: Derivation and analysis of a high-resolution estimate of global permafrost zonation, The Cryosphere, 6, 221-233, https://doi.org/10.5194/tc-6-221-2012, 2012.

640 Hausfather, Z., Marvel, K., Schmidt, G. A., Nielsen-Gammon, J. W., and Zelinka, M.: Climate simulations: recognize the 'hot model' problem, Nature, 605, 26-29, https://doi.org/10.1038/d41586-022-01192-2, 2022.

Hengl, T., de Jesus, J. M., MacMillan, R. A., Batjes, N. H., Heuvelink, G. B., Ribeiro, E., Samuel-Rosa, A., Kempen, B., Leenaars, J. G., Walsh, M. G., and Gonzalez, M. R.: SoilGrids1km--global soil information based on automated mapping, PLoS One, 9, e105992, https://doi.org/10.1371/journal.pone.0105992, 2014.

645 Henry, M., and Merlis, T. M.: Forcing Dependence of Atmospheric Lapse Rate Changes Dominates Residual Polar Warming in Solar Radiation Management Climate Scenarios, Geophys. Res. Lett., 47, e2020GL087929, https://doi.org/10.1029/2020GL087929, 2020.

Henry, M., Merlis, T. M., Lutsko, N. J., and Rose, B. E. J.: Decomposing the Drivers of Polar Amplification with a Single-Column Model, J. Climate, 34, 2355-2365, https://doi.org/10.1175/JCLI-D-20-0178.1, 2021.

650 Huang, Y., Guenet, B., Wang, Y. L., and Ciais, P.: Global Simulation and Evaluation of Soil Organic Matter and Microbial Carbon and Nitrogen Stocks Using the Microbial Decomposition Model ORCHIMIC v2.0, Global Biogeochem. Cy., 35,

e2020GB006836, https://doi.org/10.1029/2020GB006836, 2021.

Hugelius, G., Bockheim, J. G., Camill, P., Elberling, B., Grosse, G., Harden, J. W., Johnson, K., Jorgenson, T., Koven, C.

655   D., Kuhry, P., Michaelson, G., Mishra, U., Palmtag, J., Ping, C. L., O'Donnell, J., Schirrmeister, L., Schuur, E. A. G.,

Sheng, Y., Smith, L. C., Strauss, J., and Yu, Z.: A new data set for estimating organic carbon storage to 3 m depth in soils

of the northern circumpolar permafrost region, Earth System Science Data, 5, 393-402, https://doi.org/10.5194/essd-5-

393-2013, 2013.

Hugelius, G., Strauss, J., Zubrzycki, S., Harden, J. W., Schuur, E. A. G., Ping, C. L., Schirrmeister, L., Grosse, G.,

Michaelson, G. J., Koven, C. D., O'Donnell, J. A., Elberling, B., Mishra, U., Camill, P., Yu, Z., Palmtag, J., and Kuhry,

660   P.: Estimated stocks of circumpolar permafrost carbon with quantified uncertainty ranges and identified data gaps,

Biogeosciences, 11, 6573-6593, https://doi.org/10.5194/bg-11-6573-2014, 2014.

Ito, A., Hajima, T., Lawrence, D. M., Brovkin, V., Delire, C., Guenet, B., Jones, C. D., Malyshev, S., Materia, S.,

McDermid, S. P., Peano, D., Pongratz, J., Robertson, E., Shevliakova, E., Vuichard, N., Warlind, D., Wiltshire, A., and

Ziehn, T.: Soil carbon sequestration simulated in CMIP6-LUMIP models: implications for climatic mitigation, Environ.

665   Res. Lett., 15, 124061, https://doi.org/10.1088/1748-9326/abc912, 2020.

Jiang, J., Cao, L., MacMartin, D. G., Simpson, I. R., Kravitz, B., Cheng, W., Visioni, D., Tilmes, S., Richter, J. H., and

Mills, M. J.: Stratospheric Sulfate Aerosol Geoengineering Could Alter the High‐Latitude Seasonal Cycle, Geophys.

Res. Lett., 46, 14153-14163, https://doi.org/10.1029/2019GL085758, 2019.

Jones, A., Haywood, J. M., Jones, A. C., Tilmes, S., Kravitz, B., and Robock, A.: North Atlantic Oscillation response in

670   GeoMIP experiments G6solar and G6sulfur: why detailed modelling is needed for understanding regional implications of

solar radiation management, Atmos. Chem. Phys., 21, 1287-1304, https://doi.org/10.5194/acp-21-1287-2021, 2021.

Keith, D. W., Wagner, G., and Zabel, C. L.: Solar geoengineering reduces atmospheric carbon burden, Nat. Clim. Change, 7,

617-619, https://doi.org/10.1038/nclimate3376, 2017.

Kleinen, T., and Brovkin, V.: Pathway-dependent fate of permafrost region carbon, Environ. Res. Lett., 13, 094001,

675   https://doi.org/10.1088/1748-9326/aad824, 2018.

Koven, C. D., Friedlingstein, P., Ciais, P., Khvorostyanov, D., Krinner, G., and Tarnocai, C.: On the formation of high-

latitude soil carbon stocks: Effects of cryoturbation and insulation by organic matter in a land surface model, Geophys.

Res. Lett., 36, L21501, https://doi.org/10.1029/2009GL040150, 2009.

Koven, C. D., Ringeval, B., Friedlingstein, P., Ciais, P., Cadule, P., Khvorostyanov, D., Krinner, G., and Tarnocai, C.:

680   Permafrost carbon-climate feedbacks accelerate global warming, P. Natl. Acad. Sci. Usa., 108, 14769-14774,

https://doi.org/10.1073/pnas.1103910108, 2011.

Koven, C. D., Lawrence, D. M., and Riley, W. J.: Permafrost carbon−climate feedback is sensitive to

deep soil carbon decomposability but not deep soil nitrogen dynamics, Proceedings of the National Academy of Sciences,

112, 3752-3757, https://doi.org/10.1073/pnas.1415123112, 2015.

685   Koven, C. D., Hugelius, G., Lawrence, D. M., and Wieder, W. R.: Higher climatological temperature sensitivity of soil

carbon in cold than warm climates, Nat. Clim. Change, 7, 817-822, https://doi.org/10.1038/nclimate3421, 2017.

Krause, A., Kloster, S., Wilkenskjeld, S., and Paeth, H.: The sensitivity of global wildfires to simulated past, present, and

future lightning frequency, Journal of Geophysical Research: Biogeosciences, 119, 312-322,

https://doi.org/10.1002/2013JG002502, 2014.

690   Kravitz, B., Robock, A., Boucher, O., Schmidt, H., Taylor, K. E., Stenchikov, G., and Schulz, M.: The Geoengineering

Model Intercomparison Project (GeoMIP), Atmos. Sci. Lett., 12, 162-167, https://doi.org/10.1002/asl.316, 2011.

Kravitz, B., Robock, A., Forster, P. M., Haywood, J. M., Lawrence, M. G., and Schmidt, H.: An overview of the

Geoengineering Model Intercomparison Project (GeoMIP), Journal of Geophysical Research: Atmospheres, 118, 13,103-

13,107, https://doi.org/10.1002/2013JD020569, 2013a.

695   Kravitz, B., Rasch, P. J., Forster, P. M., Andrews, T., Cole, J. N. S., Irvine, P. J., Ji, D., Kristjánsson, J. E., Moore, J. C.,

Muri, H., Niemeier, U., Robock, A., Singh, B., Tilmes, S., Watanabe, S., and Yoon, J.: An energetic perspective on

hydrological cycle changes in the Geoengineering Model Intercomparison Project, Journal of Geophysical Research:

Atmospheres, 118, 13,087-13,102, https://doi.org/10.1002/2013JD020502, 2013b.

Kravitz, B., Robock, A., Tilmes, S., Boucher, O., English, J. M., Irvine, P. J., Jones, A., Lawrence, M. G., MacCracken, M.,

700   Muri, H., Moore, J. C., Niemeier, U., Phipps, S. J., Sillmann, J., Storelvmo, T., Wang, H., and Watanabe, S.: The

Geoengineering Model Intercomparison Project Phase 6 (GeoMIP6): simulation design and preliminary results, Geosci.

Model Dev., 8, 3379-3392, https://doi.org/10.5194/gmd-8-3379-2015, 2015.

Kravitz, B., MacMartin, D. G., Wang, H., and Rasch, P. J.: Geoengineering as a design problem, Earth Syst. Dynam., 7, 469-

497, https://doi.org/10.5194/esd-7-469-2016, 2016.

705   Kravitz, B., MacMartin, D. G., Tilmes, S., Richter, J. H., Mills, M. J., Cheng, W., Dagon, K., Glanville, A. S., Lamarque, J.

F., Simpson, I. R., Tribbia, J., and Vitt, F.: Comparing Surface and Stratospheric Impacts of Geoengineering with

Different SO_2 Injection Strategies, Journal of Geophysical Research: Atmospheres, 124, 7900-7918,

https://doi.org/10.1029/2019JD030329, 2019.

Krinner, G., Viovy, N., de Noblet-Ducoudré, N., Ogée, J., Polcher, J., Friedlingstein, P., Ciais, P., Sitch, S., and Prentice, I.

710   C.: A dynamic global vegetation model for studies of the coupled atmosphere-biosphere system, Global Biogeochem.

Cy., 19, GB1015, https://doi.org/10.1029/2003GB002199, 2005.

Lauritzen, P. H., Nair, R. D., Herrington, A. R., Callaghan, P., Goldhaber, S., Dennis, J. M., Bacmeister, J. T., Eaton, B. E.,

Zarzycki, C. M., Taylor, M. A., Ullrich, P. A., Dubos, T., Gettelman, A., Neale, R. B., Dobbins, B., Reed, K. A., Hannay,

C., Medeiros, B., Benedict, J. J., and Tribbia, J. J.: NCAR Release of CAM-SE in CESM2.0: A Reformulation of the

715   Spectral Element Dynamical Core in Dry-Mass Vertical Coordinates With Comprehensive Treatment of Condensates and

Energy, J. Adv. Model. Earth Sy., 10, 1537-1570, https://doi.org/10.1029/2017MS001257, 2018.

Lawrence, D. M., and Slater, A. G.: A projection of severe near-surface permafrost degradation during the 21st century, Geophys. Res. Lett., 32, https://doi.org/10.1029/2005GL025080, 2005.

Lawrence, D. M., Slater, A. G., and Swenson, S. C.: Simulation of Present-Day and Future Permafrost and Seasonally

720   Frozen Ground Conditions in CCSM4, J. Climate, 25, 2207-2225, https://doi.org/10.1175/JCLI-D-11-00334.1, 2012.

Lawrence, D. M., Fisher, R. A., Koven, C. D., Oleson, K. W., Swenson, S. C., Bonan, G., Collier, N., Ghimire, B., Kampenhout, L., Kennedy, D., Kluzek, E., Lawrence, P. J., Li, F., Li, H., Lombardozzi, D., Riley, W. J., Sacks, W. J., Shi, M., Vertenstein, M., Wieder, W. R., Xu, C., Ali, A. A., Badger, A. M., Bisht, G., Broeke, M., Brunke, M. A., Burns, S. P., Buzan, J., Clark, M., Craig, A., Dahlin, K., Drewniak, B., Fisher, J. B., Flanner, M., Fox, A. M., Gentine, P.,

725   Hoffman, F., Keppel Aleks, G., Knox, R., Kumar, S., Lenaerts, J., Leung, L. R., Lipscomb, W. H., Lu, Y., Pandey, A., Pelletier, J. D., Perket, J., Randerson, J. T., Ricciuto, D. M., Sanderson, B. M., Slater, A., Subin, Z. M., Tang, J., Thomas, R. Q., Val Martin, M., and Zeng, X.: The Community Land Model Version 5: Description of New Features, Benchmarking, and Impact of Forcing Uncertainty, J. Adv. Model. Earth Sy., 11, 4245-4287, https://doi.org/10.1029/2018MS001583, 2019.

730   Lee, H., Ekici, A., Tjiputra, J., Muri, H., Chadburn, S. E., Lawrence, D. M., and Schwinger, J.: The Response of Permafrost and High‐Latitude Ecosystems Under Large‐Scale Stratospheric Aerosol Injection and Its Termination, Earth's Future, 7, 605-614, https://doi.org/10.1029/2018EF001146, 2019.

Lee, H., Muri, H., Ekici, A., Tjiputra, J., and Schwinger, J.: The response of terrestrial ecosystem carbon cycling under different aerosol-based radiation management geoengineering, Earth Syst. Dynam., 12, 313-326,

735   https://doi.org/10.5194/esd-12-313-2021, 2021.

Lenton, T. M., Held, H., Kriegler, E., Hall, J. W., Lucht, W., Rahmstorf, S., and Schellnhuber, H. J.: Tipping elements in the Earth's climate system, Proc. Natl. Acad. Sci. USA., 105, 1786-1793, https://doi.org/10.1073/pnas.0705414105, 2008.

MacDougall, A. H., Avis, C. A., and Weaver, A. J.: Significant contribution to climate warming from the permafrost carbon feedback, Nat. Geosci., 5, 719-721, https://doi.org/10.1038/ngeo1573, 2012.

740   MacDougall, A. H., and Knutti, R.: Projecting the release of carbon from permafrost soils using a perturbed parameter ensemble modelling approach, Biogeosciences, 13, 2123-2136, https://doi.org/10.5194/bg-13-2123-2016, 2016.

Mauritsen, T., Bader, J., Becker, T., Behrens, J., Bittner, M., Brokopf, R., Brovkin, V., Claussen, M., Crueger, T., Esch, M., Fast, I., Fiedler, S., Fläschner, D., Gayler, V., Giorgetta, M., Goll, D. S., Haak, H., Hagemann, S., Hedemann, C., Hohenegger, C., Ilyina, T., Jahns, T., Jimenéz De La Cuesta, D., Jungclaus, J., Kleinen, T., Kloster, S., Kracher, D.,

745   Kinne, S., Kleberg, D., Lasslop, G., Kornblueh, L., Marotzke, J., Matei, D., Meraner, K., Mikolajewicz, U., Modali, K., Möbis, B., Müller, W. A., Nabel, J. E. M. S., Nam, C. C. W., Notz, D., Nyawira, S. S., Paulsen, H., Peters, K., Pincus, R., Pohlmann, H., Pongratz, J., Popp, M., Raddatz, T. J., Rast, S., Redler, R., Reick, C. H., Rohrschneider, T., Schemann, V.,

Schmidt, H., Schnur, R., Schulzweida, U., Six, K. D., Stein, L., Stemmler, I., Stevens, B., Storch, J. S., Tian, F., Voigt, A., Vrese, P., Wieners, K. H., Wilkenskjeld, S., Winkler, A., and Roeckner, E.: Developments in the MPI-M Earth

750   System Model version 1.2 (MPI-ESM1.2) and Its Response to Increasing CO_2, J. Adv. Model. Earth Sy., 11, 998-1038, https://doi.org/10.1029/2018MS001400, 2019.

McGuire, A. D., Koven, C., Lawrence, D. M., Clein, J. S., Xia, J., Beer, C., Burke, E., Chen, G., Chen, X., Delire, C., Jafarov, E., MacDougall, A. H., Marchenko, S., Nicolsky, D., Peng, S., Rinke, A., Saito, K., Zhang, W., Alkama, R., Bohn, T. J., Ciais, P., Decharme, B., Ekici, A., Gouttevin, I., Hajima, T., Hayes, D. J., Ji, D., Krinner, G., Lettenmaier, D.

755   P., Luo, Y., Miller, P. A., Moore, J. C., Romanovsky, V., Schädel, C., Schaefer, K., Schuur, E. A. G., Smith, B., Sueyoshi, T., and Zhuang, Q.: Variability in the sensitivity among model simulations of permafrost and carbon dynamics in the permafrost region between 1960 and 2009, Global Biogeochem. Cy., 30, 1015-1037, https://doi.org/10.1002/2016GB005405, 2016.

McGuire, A. D., Lawrence, D. M., Koven, C., Clein, J. S., Burke, E., Chen, G., Jafarov, E., MacDougall, A. H., Marchenko,

760   S., Nicolsky, D., Peng, S., Rinke, A., Ciais, P., Gouttevin, I., Hayes, D. J., Ji, D., Krinner, G., Moore, J. C., Romanovsky, V., Schädel, C., Schaefer, K., Schuur, E. A. G., and Zhuang, Q.: Dependence of the evolution of carbon dynamics in the northern permafrost region on the trajectory of climate change, Proceedings of the National Academy of Sciences, 115, 3882-3887, https://doi.org/10.1073/pnas.1719903115, 2018.

Meehl, G. A., Senior, C. A., Eyring, V., Flato, G., Lamarque, J. F., Stouffer, R. J., Taylor, K. E., and Schlund, M.: Context

765   for interpreting equilibrium climate sensitivity and transient climate response from the CMIP6 Earth system models, Sci Adv, 6, eaba1981, https://doi.org/10.1126/sciadv.aba1981, 2020.

Meinshausen, M., Nicholls, Z. R. J., Lewis, J., Gidden, M. J., Vogel, E., Freund, M., Beyerle, U., Gessner, C., Nauels, A., Bauer, N., Canadell, J. G., Daniel, J. S., John, A., Krummel, P. B., Luderer, G., Meinshausen, N., Montzka, S. A., Rayner, P. J., Reimann, S., Smith, S. J., van den Berg, M., Velders, G. J. M., Vollmer, M. K., and Wang, R. H. J.: The shared

770   socio-economic pathway (SSP) greenhouse gas concentrations and their extensions to 2500, Geosci. Model Dev., 13, 3571–3605, https://doi.org/10.5194/gmd-13-3571-2020, 2020.

Melnikova, I., Boucher, O., Cadule, P., Ciais, P., Gasser, T., Quilcaille, Y., Shiogama, H., Tachiiri, K., Yokohata, T., and Tanaka, K.: Carbon Cycle Response to Temperature Overshoot Beyond 2°C: An Analysis of CMIP6 Models, Earth's Future, 9, e2020EF001967, https://doi.org/10.1029/2020EF001967, 2021.

775 Muri, H., Niemeier, U., and Kristjánsson, J. E.: Tropical rainforest response to marine sky brightening climate engineering, Geophys. Res. Lett., 42, 2951-2960, https://doi.org/10.1002/2015GL063363, 2015.

Muri, H., Tjiputra, J., Otterå, O. H., Adakudlu, M., Lauvset, S. K., Grini, A., Schulz, M., Niemeier, U., and Kristjánsson, J. E.: Climate Response to Aerosol Geoengineering: A Multimethod Comparison, J. Climate, 31, 6319-6340, https://doi.org/10.1175/JCLI-D-17-0620.1, 2018.

780 NCSCDv2: Northern Circumpolar Soil Carbon Database version 2, available at: https://bolin.su.se/data/ncscd/, last access,
12 January, 2022.

Niemeier, U., Schmidt, H., Alterskjaer, K., and Kristjánsson, J. E.: Solar irradiance reduction via climate engineering:
Impact of different techniques on the energy balance and the hydrological cycle, Journal of Geophysical Research:
Atmospheres, 118, 11,905-11,917, https://doi.org/10.1002/2013JD020445, 2013.

785 Obu, J., Westermann, S., Bartsch, A., Berdnikov, N., Christiansen, H. H., Dashtseren, A., Delaloye, R., Elberling, B.,
Etzelmüller, B., Kholodov, A., Khomutov, A., Kääb, A., Leibman, M. O., Lewkowicz, A. G., Panda, S. K., Romanovsky,
V., Way, R. G., Westergaard-Nielsen, A., Wu, T., Yamkhin, J., and Zou, D.: Northern Hemisphere permafrost map based
on TTOP modelling for 2000-2016 at 1 km2 scale, Earth-Sci. Rev., 193, 299-316,
https://doi.org/10.1016/j.earscirev.2019.04.023, 2019.

790 O'Neill, B. C., Tebaldi, C., van Vuuren, D. P., Eyring, V., Friedlingstein, P., Hurtt, G., Knutti, R., Kriegler, E., Lamarque, J.,
Lowe, J., Meehl, G. A., Moss, R., Riahi, K., and Sanderson, B. M.: The Scenario Model Intercomparison Project
(ScenarioMIP) for CMIP6, Geosci. Model Dev., 9, 3461-3482, https://doi.org/10.5194/gmd-9-3461-2016, 2016.

Opfergelt, S.: The next generation of climate model should account for the evolution of mineral-organic interactions with
permafrost thaw, Environ. Res. Lett., 15, 091003, https://doi.org/10.1088/1748-9326/ab9a6d, 2020.

795 Peng, S., Ciais, P., Krinner, G., Wang, T., Gouttevin, I., McGuire, A. D., Lawrence, D., Burke, E., Chen, X., Decharme, B.,
Koven, C., MacDougall, A., Rinke, A., Saito, K., Zhang, W., Alkama, R., Bohn, T. J., Delire, C., Hajima, T., Ji, D.,
Lettenmaier, D. P., Miller, P. A., Moore, J. C., Smith, B., and Sueyoshi, T.: Simulated high-latitude soil thermal dynamics
during the past 4 decades, The Cryosphere, 10, 179-192, https://doi.org/10.5194/tc-10-179-2016, 2016.

Plazzotta, M., Séférian, R., and Douville, H.: Impact of Solar Radiation Modification on Allowable CO2 Emissions: What
800 Can We Learn From Multimodel Simulations? Earth's Future, 7, 664-676, https://doi.org/10.1029/2019EF001165, 2019.

Reick, C. H., Gayler, V., Goll, D., Hagemann, S., Heidkamp, M., Nabel, J. E. M. S., Raddatz, T., Roeckner, E., Schnur, R.,
and Wilkenskjeld, S.: JSBACH 3 - The land component of the MPI Earth System Model: documentation of version 3.2,
Hamburg: MPI für Meteorologie, 287 pp., https://doi:10.17617/2.3279802, 2021.

Russotto, R. D., and Ackerman, T. P.: Energy transport, polar amplification, and ITCZ shifts in the GeoMIP G1 ensemble,
805 Atmos. Chem. Phys., 18, 2287-2305, https://doi.org/10.5194/acp-18-2287-2018, 2018.

Schmidt, H., Alterskjær, K., Bou Karam, D., Boucher, O., Jones, A., Kristjánsson, J. E., Niemeier, U., Schulz, M., Aaheim,
A., Benduhn, F., Lawrence, M., and Timmreck, C.: Solar irradiance reduction to counteract radiative forcing from a
quadrupling of CO2: climate responses simulated by four earth system models, Earth Syst. Dynam., 3, 63-78,
https://doi.org/10.5194/esd-3-63-2012, 2012.

810 Schneider Von Deimling, T., Meinshausen, M., Levermann, A., Huber, V., Frieler, K., Lawrence, D. M., and Brovkin, V.:
Estimating the near-surface permafrost-carbon feedback on global warming, Biogeosciences, 9, 649-665,

https://doi.org/10.5194/bg-9-649-2012, 2012.

Schuur, E. A. G., Bockheim, J., Canadell, J. G., Euskirchen, E., Field, C. B., Goryachkin, S. V., Hagemann, S., Kuhry, P., Lafleur, P. M., Lee, H., Mazhitova, G., Nelson, F. E., Rinke, A., Romanovsky, V. E., Shiklomanov, N., Tarnocai, C.,

815   Venevsky, S., Vogel, J. G., and Zimov, S. A.: Vulnerability of Permafrost Carbon to Climate Change: Implications for the Global Carbon Cycle, BioScience, 58, 701-714, https://doi.org/10.1641/B580807, 2008.

Schuur, E. A. G., McGuire, A. D., Schädel, C., Grosse, G., Harden, J. W., Hayes, D. J., Hugelius, G., Koven, C. D., Kuhry, P., Lawrence, D. M., Natali, S. M., Olefeldt, D., Romanovsky, V. E., Schaefer, K., Turetsky, M. R., Treat, C. C., and Vonk, J. E.: Climate change and the permafrost carbon feedback, Nature, 520, 171-179,

820   https://doi.org/10.1038/nature14338, 2015.

Séférian, R., Nabat, P., Michou, M., Saint-Martin, D., Voldoire, A., Colin, J., Decharme, B., Delire, C., Berthet, S., Chevallier, M., Senesi, S., Franchisteguy, L., Vial, J., Mallet, M., Joetzjer, E., Geoffroy, O., Gueremy, J. F., Moine, M. P., Msadek, R., Ribes, A., Rocher, M., Roehrig, R., Salas-y-Melia, D., Sanchez, E., Terray, L., Valcke, S., Waldman, R., Aumont, O., Bopp, L., Deshayes, J., Ethe, C., and Madec, G.: Evaluation of CNRM Earth System Model, CNRM-ESM2-

825   1: Role of Earth System Processes in Present-Day and Future Climate, J. Adv. Model. Earth Sy., 11, 4182-4227, https://doi.org/10.1029/2019MS001791, 2019.

Sellar, A. A., Jones, C. G., Mulcahy, J. P., Tang, Y., Yool, A., Wiltshire, A., O'Connor, F. M., Stringer, M., Hill, R., Palmieri, J., Woodward, S., Mora, L., Kuhlbrodt, T., Rumbold, S. T., Kelley, D. I., Ellis, R., Johnson, C. E., Walton, J., Abraham, N. L., Andrews, M. B., Andrews, T., Archibald, A. T., Berthou, S., Burke, E., Blockley, E., Carslaw, K., Dalvi,

830   M., Edwards, J., Folberth, G. A., Gedney, N., Griffiths, P. T., Harper, A. B., Hendry, M. A., Hewitt, A. J., Johnson, B., Jones, A., Jones, C. D., Keeble, J., Liddicoat, S., Morgenstern, O., Parker, R. J., Predoi, V., Robertson, E., Siahaan, A., Smith, R. S., Swaminathan, R., Woodhouse, M. T., Zeng, G., and Zerroukat, M.: UKESM1: Description and Evaluation of the U.K. Earth System Model, J. Adv. Model. Earth Sy., 11, 4513-4558, https://doi.org/10.1029/2019MS001739, 2019.

Sellers, P. J., Hall, F. G., Kelly, R. D., Black, A., Baldocchi, D., Berry, J., Ryan, M., Ranson, K. J., Crill, P. M., Lettenmaier,

835   D. P., Margolis, H., Cihlar, J., Newcomer, J., Fitzjarrald, D., Jarvis, P. G., Gower, S. T., Halliwell, D., Williams, D., Goodison, B., Wickland, D. E., and Guertin, F. E.: BOREAS in 1997: Experiment overview, scientific results, and future directions, Journal of Geophysical Research: Atmospheres, 102, 28731-28769, https://doi.org/10.1029/97JD03300, 1997.

Serreze, M. C., and Barry, R. G.: Processes and impacts of Arctic amplification: A research synthesis, Global Planet. Change, 77, 85-96, https://doi.org/10.1016/j.gloplacha.2011.03.004, 2011.

840   Shindell, D. T.: Dynamic winter climate response to large tropical volcanic eruptions since 1600, Journal of Geophysical Research, 109, D05104, https://doi.org/10.1029/2003JD004151, 2004.

Shu, S., Jain, A. K., Koven, C. D., and Mishra, U.: Estimation of Permafrost SOC Stock and Turnover Time Using a Land Surface Model with Vertical Heterogeneity of Permafrost Soils, Global Biogeochem. Cy., 34, e2020GB006585,

https://doi.org/10.1029/2020GB006585, 2020.

845   Simpson, I. R., Tilmes, S., Richter, J. H., Kravitz, B., MacMartin, D. G., Mills, M. J., Fasullo, J. T., and Pendergrass, A. G.:

The Regional Hydroclimate Response to Stratospheric Sulfate Geoengineering and the Role of Stratospheric Heating,

Journal of Geophysical Research: Atmospheres, 124, 12587-12616, https://doi.org/10.1029/2019JD031093, 2019.

Slater, A. G., and Lawrence, D. M.: Diagnosing Present and Future Permafrost from Climate Models, J. Climate, 26, 5608-

5623, https://doi.org/10.1175/JCLI-D-12-00341.1, 2013.

850   Strauss, J., Schirrmeister, L., Grosse, G., Fortier, D., Hugelius, G., Knoblauch, C., Romanovsky, V., Schädel, C., Schneider

Von Deimling, T., Schuur, E. A. G., Shmelev, D., Ulrich, M., and Veremeeva, A.: Deep Yedoma permafrost: A synthesis

of depositional characteristics and carbon vulnerability, Earth-Sci. Rev., 172, 75-86,

https://doi.org/10.1016/j.earscirev.2017.07.007, 2017.

Tarnocai, C., Canadell, J. G., Schuur, E. A. G., Kuhry, P., Mazhitova, G., and Zimov, S.: Soil organic carbon pools in the

855   northern circumpolar permafrost region, Global Biogeochem. Cy., 23, GB2023, https://doi.org/10.1029/2008GB003327,

2009.

Taylor, K. E., Stouffer, R. J., and Meehl, G. A.: An Overview of CMIP5 and the Experiment Design, B. Am. Meteorol. Soc.,

93, 485-498, https://doi.org/10.1175/BAMS-D-11-00094.1, 2012.

Tilmes, S., Fasullo, J., Lamarque, J., Marsh, D. R., Mills, M., Alterskjaer, K., Muri, H., Kristjánsson, J. E., Boucher, O.,

860   Schulz, M., Cole, J. N. S., Curry, C. L., Jones, A., Haywood, J., Irvine, P. J., Ji, D., Moore, J. C., Karam, D. B., Kravitz,

B., Rasch, P. J., Singh, B., Yoon, J., Niemeier, U., Schmidt, H., Robock, A., Yang, S., and Watanabe, S.: The

hydrological impact of geoengineering in the Geoengineering Model Intercomparison Project (GeoMIP), Journal of

Geophysical Research: Atmospheres, 118, 11,036-11,058, https://doi.org/10.1002/jgrd.50868, 2013.

Tjiputra, J. F., Grini, A., and Lee, H.: Impact of idealized future stratospheric aerosol injection on the large-scale ocean and

865   land carbon cycles, Journal of Geophysical Research: Biogeosciences, 121, 2-27, https://doi.org/10.1002/2015JG003045,

2016.

Todd-Brown, K. E. O., Randerson, J. T., Post, W. M., Hoffman, F. M., Tarnocai, C., Schuur, E. A. G., and Allison, S. D.:

Causes of variation in soil carbon simulations from CMIP5 Earth system models and comparison with observations,

Biogeosciences, 10, 1717-1736, https://doi.org/10.5194/bg-10-1717-2013, 2013.

870   Todd-Brown, K. E. O., Randerson, J. T., Hopkins, F., Arora, V., Hajima, T., Jones, C., Shevliakova, E., Tjiputra, J., Volodin,

E., Wu, T., Zhang, Q., and Allison, S. D.: Changes in soil organic carbon storage predicted by Earth system models

during the 21st century, Biogeosciences, 11, 2341-2356, https://doi.org/10.5194/bg-11-2341-2014, 2014.

Turetsky, M. R., Benscoter, B., Page, S., Rein, G., van der Werf, G. R., and Watts, A.: Global vulnerability of peatlands to

fire and carbon loss, Nat. Geosci., 8, 11-14, https://doi.org/10.1038/ngeo2325, 2015.

875   Varney, R. M., Chadburn, S. E., Friedlingstein, P., Burke, E. J., Koven, C. D., Hugelius, G., and Cox, P. M.: A spatial

emergent constraint on the sensitivity of soil carbon turnover to global warming, Nat. Commun., 11, 1-8, https://doi.org/10.1038/s41467-020-19208-8, 2020.

Varney, R. M., Chadburn, S. E., Burke, E. J., and Cox, P. M.: Evaluation of soil carbon simulation in CMIP6 Earth System Models, [preprint], https://doi.org/10.5194/bg-2022-13, 24 Jan 2022

880   Veraverbeke, S., Rogers, B. M., Goulden, M. L., Jandt, R. R., Miller, C. E., Wiggins, E. B., and Randerson, J. T.: Lightning as a major driver of recent large fire years in North American boreal forests, Nat. Clim. Change, 7, 529-534, https://doi.org/10.1038/nclimate3329, 2017.

Visioni, D., MacMartin, D. G., Kravitz, B., Lee, W., Simpson, I. R., and Richter, J. H.: Reduced Poleward Transport Due to Stratospheric Heating Under Stratospheric Aerosols Geoengineering, Geophys. Res. Lett., 47, e2020GL089470,

885   https://doi.org/10.1029/2020GL089470, 2020.

Visioni, D., MacMartin, D. G., Kravitz, B., Boucher, O., Jones, A., Lurton, T., Martine, M., Mills, M. J., Nabat, P., Niemeier, U., S Ef Erian, R., and Tilmes, S.: Identifying the sources of uncertainty in climate model simulations of solar radiation modification with the G6sulfur and G6solar Geoengineering Model Intercomparison Project (GeoMIP) simulations, Atmos. Chem. Phys., 21, 10039-10063, https://doi.org/10.5194/acp-21-10039-2021, 2021.

890   WCRP: CMIP6 project data, available at: https://esgf-node.llnl.gov/ search/cmip6/, last access: 12 January 2022.

Wang, W., Rinke, A., Moore, J. C., Ji, D., Cui, X., Peng, S., Lawrence, D. M., McGuire, A. D., Burke, E. J., Chen, X., Decharme, B., Koven, C., MacDougall, A., Saito, K., Zhang, W., Alkama, R., Bohn, T. J., Ciais, P., Delire, C., Gouttevin, I., Hajima, T., Krinner, G., Lettenmaier, D. P., Miller, P. A., Smith, B., Sueyoshi, T., and Sherstiukov, A. B.: Evaluation of air‐soil temperature relationships simulated by land surfacemodels during winter across the permafrost region, The

895   Cryosphere, 10, 1721-1737, https://doi.org/10.5194/tc-10-1721-2016, 2016.

Wyser, K., van Noije, T., Yang, S., von Hardenberg, J., O'Donnell, D., and Döscher, R.: On the increased climate sensitivity in the EC-Earth model from CMIP5 to CMIP6, Geosci. Model Dev., 13, 3465-3474, https://doi.org/10.5194/gmd-13-3465-2020, 2020.

Xia, L., Robock, A., Tilmes, S., and Neely III, R. R.: Stratospheric sulfate geoengineering could enhance the terrestrial

900   photosynthesis rate, Atmos. Chem. Phys., 16, 1479-1489, https://doi.org/10.5194/acp-16-1479-2016, 2016.

Yu, X., Moore, J. C., Cui, X., Rinke, A., Ji, D., Kravitz, B., and Yoon, J.: Impacts, effectiveness and regional inequalities of the GeoMIP G1 to G4 solar radiation management scenarios, Global Planet. Change, 129, 10-22, https://doi.org/10.1016/j.gloplacha.2015.02.010, 2015.

Zelinka, M. D., Klein, S. A., and Hartmann, D. L.: Computing and Partitioning Cloud Feedbacks Using Cloud Property

905   Histograms. Part II: Attribution to Changes in Cloud Amount, Altitude, and Optical Depth, J. Climate, 25, 3736-3754, https://doi.org/10.1175/JCLI-D-11-00249.1, 2012.

Zelinka, M. D., Myers, T. A., McCoy, D. T., Po Chedley, S., Caldwell, P. M., Ceppi, P., Klein, S. A., and Taylor, K. E.:

Causes of Higher Climate Sensitivity in CMIP6 Models, Geophys. Res. Lett., 47, e2019GL085782, https://doi.org/10.1029/2019GL085782, 2020.

910 Zhang, T., Heginbottom, J. A., Barry, R. G., and Brown, J.: Further statistics on the distribution of permafrost and ground ice in the Northern Hemisphere, Polar geography (1995), 24, 126-131, https://doi.org/10.1080/10889370009377692, 2000.

Zhang, Z., Moore, J. C., Huisingh, D., and Zhao, Y.: Review of geoengineering approaches to mitigating climate change, J. Clean. Prod., 103, 898-907, https://doi.org/10.1016/j.jclepro.2014.09.076, 2015.

915   **Table 1. Summary of land scheme, the constitution of soil carbon and simulations for each CMIP6 earth system model.**

Model Name	Land Scheme	Soil Layers	Soil Depth (m)	Latent Heat from Water Freeze/Thaw	Organic Soil Insulation	Carbon Dynamics*	Soil Carbon Constitution	Ensemble Member (historical/ ssp245/ ssp585/ G6solar/ G6sulfur)
CESM2-WACCM (Lauritzen et al., 2018)	CLM5 (Lawrence et al., 2019)	25	48.6	Yes	Yes	Yes	cSoil+cLitter+ cCwd	2/2/2/2/2
UKESM1-0-LL (Sellar et al., 2019)	JULES-ES-1.0 (Sellar et al., 2019)	4	3.0	Yes	Yes	No	cSoil	3/3/3/3/3
CNRM-ESM2-1 (Séférian et al., 2019)	ISBA-CTRIP (Decharme et al. 2019 ; Delire et al., 2020)	14	12.0	Yes	Yes	No	cSoil+cLitter	3/3/3/1/3
IPSL-CM6A-LR (Boucher et al., 2020)	ORCHIDEE (v2.0, Water/ Carbon/Energy Mode) (Krinner et al., 2005)	18	90.0	No	Yes	No	cSoil+cLitter	1/1/1/1/1
MPI-ESM1-2-LR (Mauritsen et al., 2019)	JSBACH 3.20 (Reick et al., 2021)	5	9.8	Yes	Yes	No	cSoil+cLitter	3/3/3/3/3

*Model vertically resolving soil organic carbon and considering cryoturbation effects on soil organic carbon.
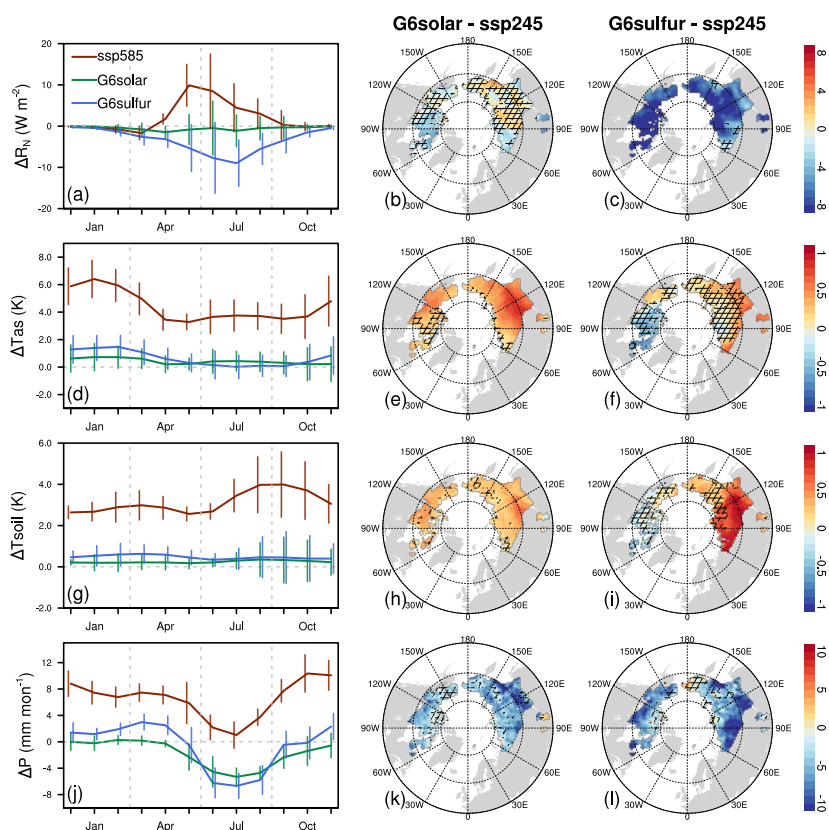
920 **Figure 1. The multi-model ensemble mean changes of surface absorbed shortwave radiation (ΔR_N; a, b, c), near-surface air temperature (ΔTas; d, e, f), 2 m soil temperature ($\Delta Tsoil$; g, h, i) and precipitation (ΔP; j, k, l) under G6solar, G6sulfur and ssp585 relative to ssp245 during the period 2080-2099 over the baseline $PF_{50\%}$ region. The left column (a, d, g, j) shows monthly climatology changes. The middle column (b, e, h, k) shows changes between G6solar and ssp245, while the right column (c, f, i, l) shows changes between G6sulfur and ssp245 in summer (June, July, and August). The vertical bar of each month in the left column denotes 1**

925 **standard error above/below multi-model ensemble mean. The hatched areas in the middle and right columns indicate where less than 80% of the models (four out of five) agree on the sign of the differences in that grid cell.**
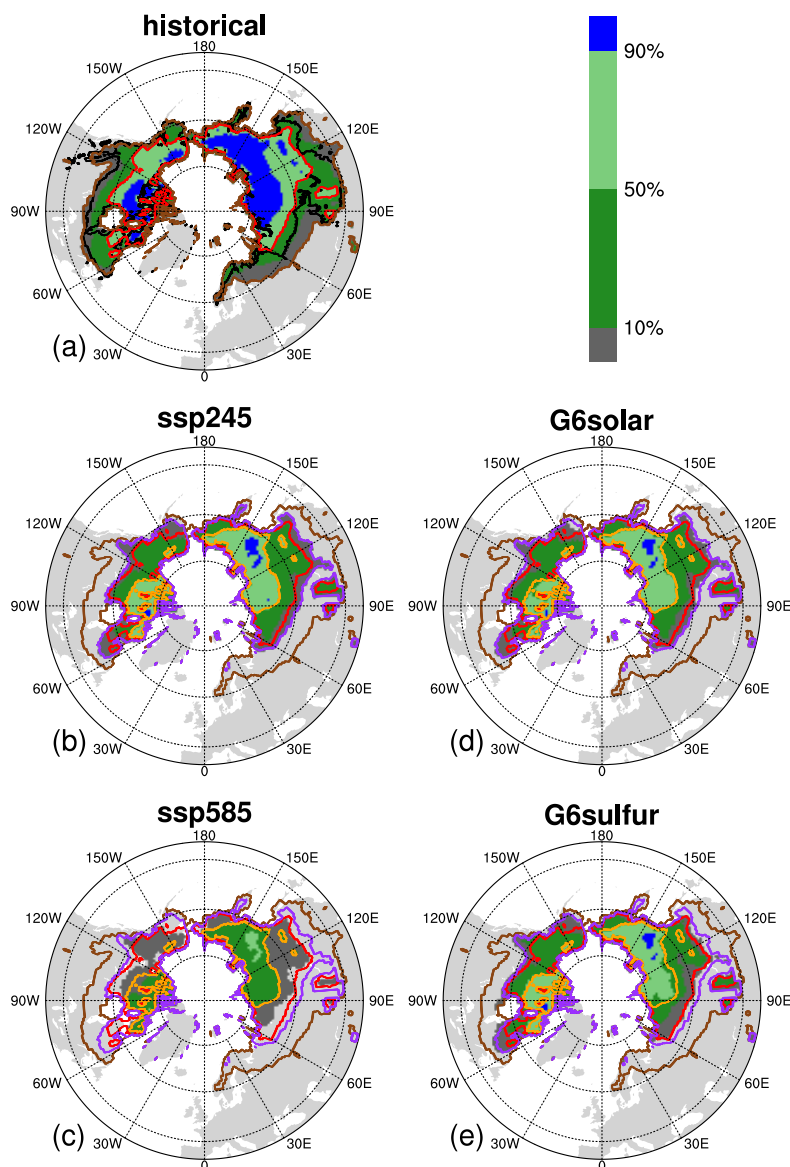
Figure 2. Multi-model ensemble mean permafrost probability (shading) and extent (curves) derived according to the observation-based MAAT-permafrost probability relationship (Chadburn et al., 2017) for the last 20 years of each experiment. The black curve in (a) is the extent of the permafrost region defined by IPA permafrost map. The brown and purple curves are the multi-model ensemble mean permafrost extents (permafrost probability ≥ 0.01) for historical and ssp245 simulations, respectively. The red and orange curves are the multi-model ensemble mean permafrost extent where the permafrost probability ≥ 0.5 for historical and ssp245 simulations, respectively.
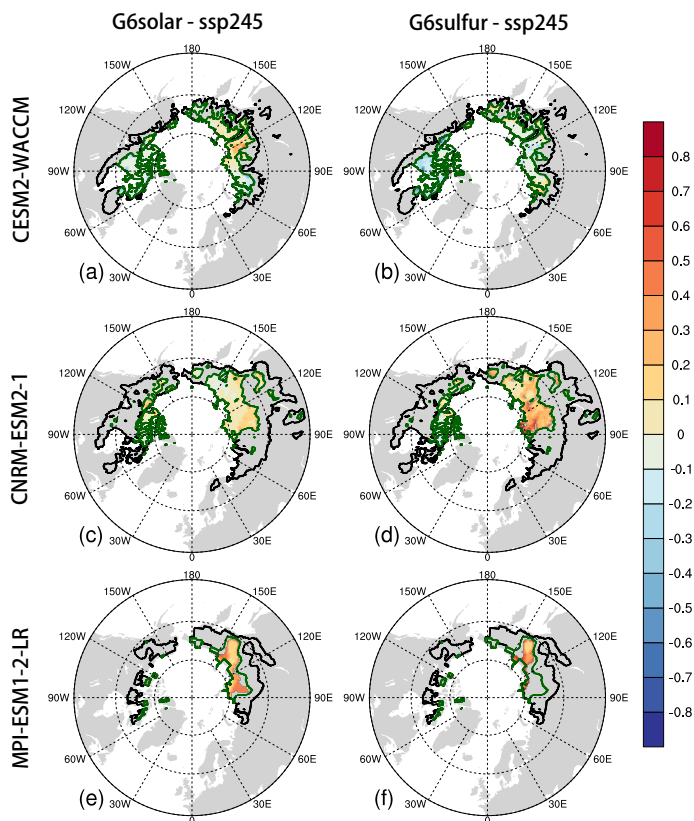
Figure 3. Changes in annual maximum active layer thickness (ALT, color filled contour) in G6solar and G6sulfur relative to ssp245 simulated by CESM2-WACCM (a, b), CNRM-ESM2-1 (c, d) and MPI-ESM1-2-LR (e, f) averaged for the period 2080-2099. The black and green lines denote the permafrost region during the period 1995-2014 in historical experiment and the period 2080-2099 in ssp245 experiment, respectively. The shaded permafrost region shows where the annual maximal ALT is less than 3 m in both G6solar and ssp245 (left column), G6sulfur and ssp245 (right column).
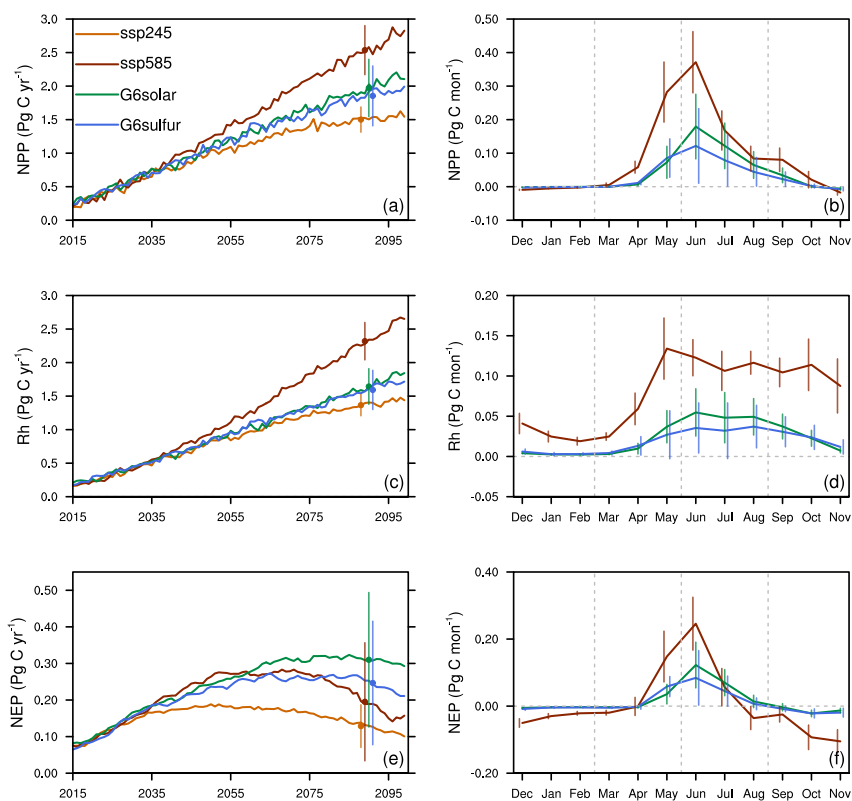
945   **Figure 4. The multi-model ensemble mean of terrestrial carbon fluxes changes over the baseline PF$_{50\%}$ region. Left column shows**
        changes in NPP (a), Rh (c) and NEP (e) relative to the baseline period 1995-2014 under ssp245, ssp585, G6solar and G6sulfur. Right
        column shows changes in monthly climatology of NPP (b), Rh (d) and NEP (f) under G6solar, G6sulfur and ssp585 relative to ssp245
        during the period 2080-2099. The vertical bar denotes 1 standard error above/below multi-model ensemble mean. In panel (e), an
        11-year running average is applied on NEP to filter its large inter-annual variation.

950
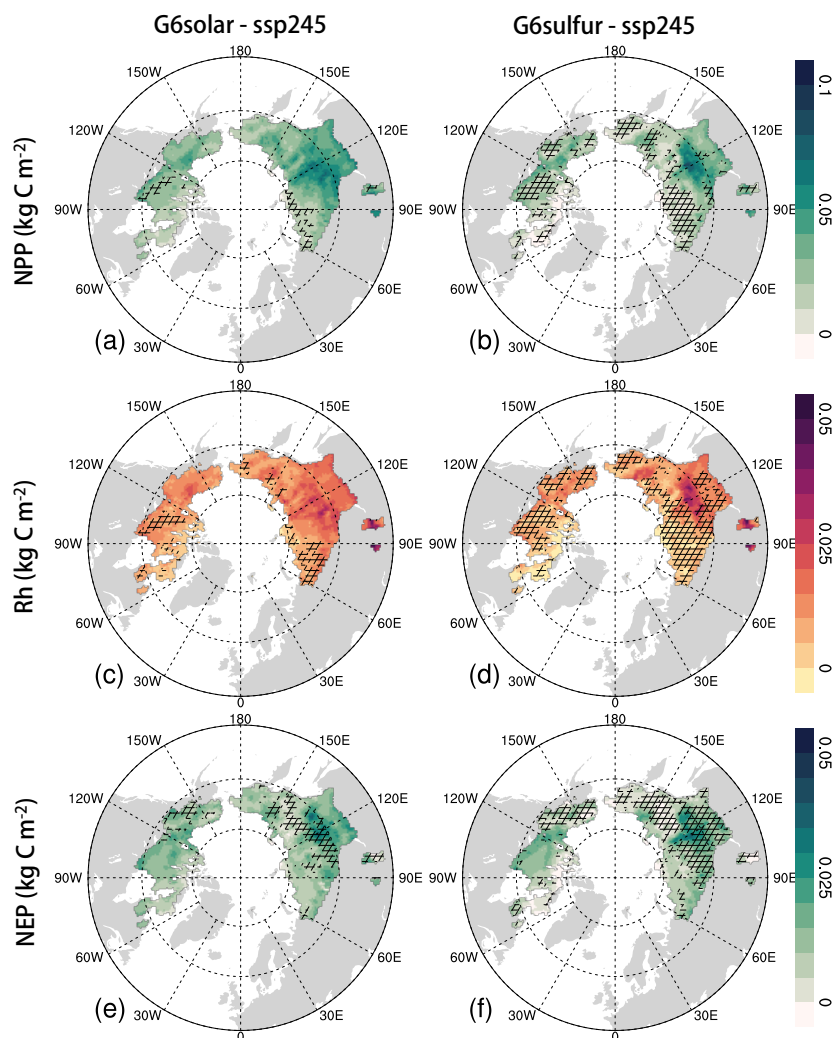
Figure 5. The multi-model ensemble mean changes in NPP (a, b), Rh (c, d), and NEP (e, f) relative to ssp245 during summer averaged for the period 2080-2099 over the baseline PF$_{50\%}$ region. Left column shows difference between G6solar and ssp245, right column shows difference between G6sulfur and ssp245. All carbon fluxes are accumulations over the summer (June, July, and August).

955   **Hatched areas indicate where less than 80% of the models (four out of five) agree on the sign of the differences in that grid cell.**
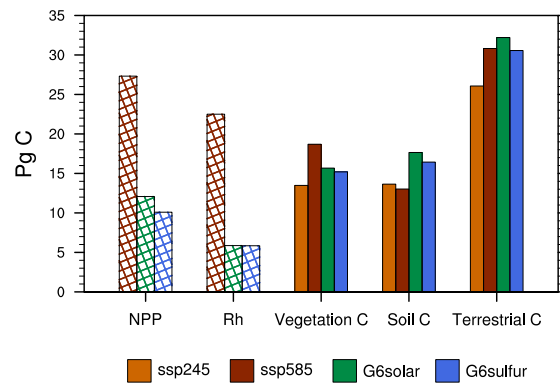
Figure 6. Multi-model ensemble mean differences in accumulated NPP and Rh relative to ssp245 for G6solar, G6sulfur and ssp585

960 **scenarios over the baseline $PF_{50\%}$ region between the periods 1995-2014 and 2080-2099 (dashed bar). Multi-model ensemble mean changes in terrestrial carbon pools over the baseline $PF_{50\%}$ region for ssp245, ssp585, G6solar and G6sulfur scenarios between the periods 1995-2014 and 2080-2099 (solid bar).**
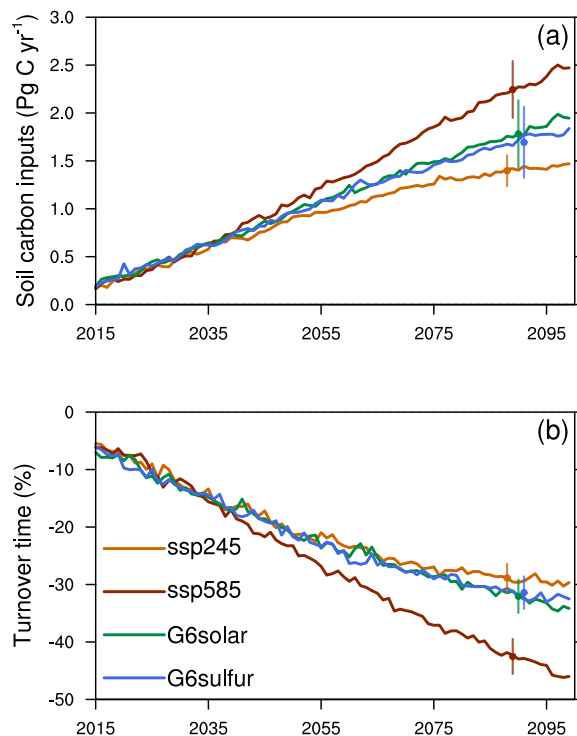
965   **Figure 7. The multi-model ensemble mean changes of soil carbon inputs (a) and percentage changes of soil turnover time (b) relative to the baseline period 1995-2014 over the baseline PF$_{50\%}$ region. The vertical bar denotes 1 standard error above/below multi-model ensemble mean for the period 2080-2099.**
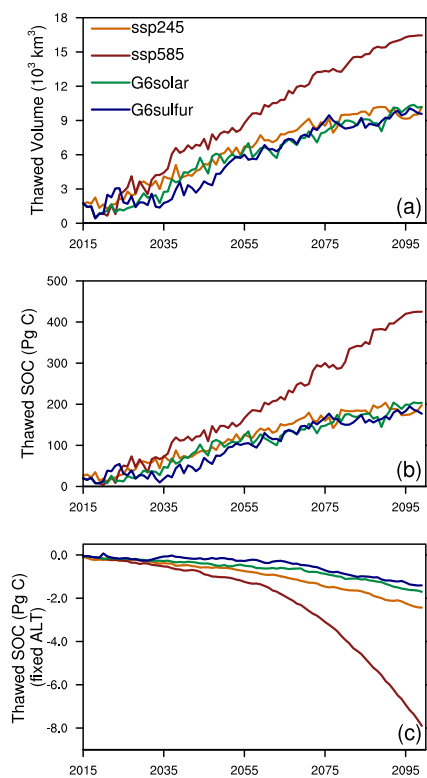
970

Figure 8. Changes in annual maximum thawed permafrost volume (a) and soil organic carbon (b, c) projected by CESM2-WACCM for ssp245, ssp585, G6solar and G6sulfur. Panel (c) shows annual maximum thawed permafrost SOC with the ALT fixed at the baseline period 1995-2014.

975